

University of New Hampshire

University of New Hampshire Scholars' Repository

Master's Theses and Capstones

Student Scholarship

Spring 2010

A vortex pair near a density-gradient interface

Nicholas S. Jenkins

University of New Hampshire, Durham

Follow this and additional works at: <https://scholars.unh.edu/thesis>

Recommended Citation

Jenkins, Nicholas S., "A vortex pair near a density-gradient interface" (2010). *Master's Theses and Capstones*. 551.

<https://scholars.unh.edu/thesis/551>

This Thesis is brought to you for free and open access by the Student Scholarship at University of New Hampshire Scholars' Repository. It has been accepted for inclusion in Master's Theses and Capstones by an authorized administrator of University of New Hampshire Scholars' Repository. For more information, please contact Scholarly.Communication@unh.edu.

A VORTEX PAIR NEAR A
DENSITY-GRADIENT INTERFACE

BY

NICHOLAS S. JENKINS

BS, University of New Hampshire, 2007

THESIS

Submitted to the University of New Hampshire
in Partial Fulfillment of
the Requirements for the Degree of

Master of Science
in
Mechanical Engineering

May, 2010

UMI Number: 1485433

All rights reserved

INFORMATION TO ALL USERS

The quality of this reproduction is dependent upon the quality of the copy submitted.

In the unlikely event that the author did not send a complete manuscript and there are missing pages, these will be noted. Also, if material had to be removed, a note will indicate the deletion.



UMI 1485433

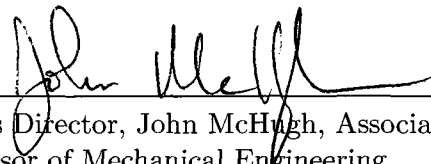
Copyright 2010 by ProQuest LLC.

All rights reserved. This edition of the work is protected against unauthorized copying under Title 17, United States Code.

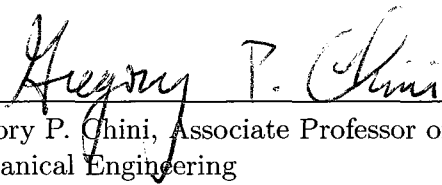


ProQuest LLC
789 East Eisenhower Parkway
P.O. Box 1346
Ann Arbor, MI 48106-1346

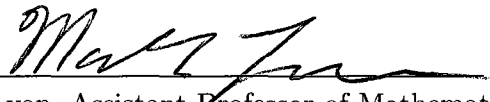
This thesis has been examined and approved.

A handwritten signature in black ink, appearing to read "John McHugh", written over a horizontal line.

Thesis Director, John McHugh, Associate
Professor of Mechanical Engineering

A handwritten signature in black ink, appearing to read "Gregory P. Chini", written over a horizontal line.

Gregory P. Chini, Associate Professor of
Mechanical Engineering

A handwritten signature in black ink, appearing to read "Mark Lyon", written over a horizontal line.

Mark Lyon, Assistant Professor of Mathematics
& Statistics

Table of Contents

Title	i
List of Tables	iv
List of Figures	v
Abstract	vi
Introduction	1
I Governing Equations	4
Re-Scaling	5
II Background State	9
Single Layer	9
Two Layer	12
III Computational Method	15
IV Initial Conditions	19
Single Vortex	19
Symmetric Vortex Pair	21
V Results	24
Single Layer	25
Mixing within a vortex	31
Two Layers	44
VI Conclusions	53
Bibliography	54

List of Tables

V.1	Input parameters from comparison to Garten, et. al. results	26
V.2	$\bar{F}_r = 4$ High resolution parameter table	27
V.3	$\bar{F}_r = 2$ Low resolution parameter table	37
V.4	$\bar{F}_r = 1.5$ Low resolution parameter table	39

List of Figures

I.1	The dimensional physical domain and the computational domain after rescaling.	6
IV.1	The initial conditions. The distance between the vortex centers is b_0 . The solid line is the release height and the dotted line is the interface height. The left figure is the physical domain with the right being representative of the domain after rescaling has occurred.	21
V.1	Contours of vorticity from the results used for comparison with Garten, et. al.	26
V.2	Contours of vorticity for the single layer case with $\bar{F}_r = 4$ and a resolution of 512x512.	28
V.3	Contours of vorticity for the single layer case with $\bar{F}_r = 4$ and a resolution of 256x256.	29
V.4	Time history of vertical position of the vortex pair for two resolutions.	30
V.5	Total potential temperature for the single layer case with $\bar{F}_r = 4$, a resolution of 512x512 and a vertical slice at $\tilde{x} = 2.9575$	33
V.6	Total potential temperature for the single layer case with $\bar{F}_r = 4$, a resolution of 512x512 and a vertical slice at $\tilde{x} = 2.9575$	34
V.7	Contours of total potential temperature for the single layer case with $\bar{F}_r = 4$ and a resolution of 512x512.	35
V.8	Contours of total potential temperature for the single layer case with $\bar{F}_r = 4$ and a resolution of 512x512.	36
V.9	Contours of vorticity for the single layer case with $\bar{F}_r = 2$ and a resolution of 256x256.	38
V.10	Contours of vorticity for the single layer case with $\bar{F}_r = 2$ and a resolution of 256x256.	39
V.11	Contours of vorticity for the single layer case with $\bar{F}_r = 1.5$ and a resolution of 256x256.	40
V.12	Contours of vorticity for the single layer case with $\bar{F}_r = 1.5$ and a resolution of 256x256.	41
V.13	Max vorticity location for single layer cases.	42
V.14	Contours of vorticity of single layer with $\bar{F}_r = 0.5$ and a resolution of 256x256.	43
V.15	Contours of vorticity for the two layer case with $\bar{F}_r = 4$ and a resolution of 512x512.	46
V.16	Contours of vorticity for the two layer with $\bar{F}_r = 4$ and a resolution of 256x256.	47

V.17 $\overline{F}_r = 4$ single layer and $\overline{F}_r = 4$ two-layer. The single layer case clearly has a higher vertical displacement as it collides with the top boundary, where the two-layer case only reaches $\hat{z} = 0.75$	48
V.18 Contours of vorticity for the two layer case with $\overline{F}_r = 2$ and a resolution of 256x256.	50
V.19 Contours of vorticity for the two layer case with $\overline{F}_r = 2$ and a resolution of 256x256.	51
V.20 $\overline{F}_r = 2$ single layer and $\overline{F}_r = 2$ two-layer. The single layer case clearly has a higher vertical displacement as it collides with the top boundary, where the two-layer case only reaches $\hat{z} = 0.75$	52

ABSTRACT

A VORTEX PAIR NEAR A DENSITY-GRADIENT INTERFACE

by

Nicholas S. Jenkins

University of New Hampshire, May, 2010

The dynamics of a vortex pair in a stratified atmosphere near a density gradient interface is considered here using direct numerical simulations. The vortex pair is released below the interface and allowed to propagate vertically toward the interface. The results show that strong vortices propagate through the interface without much change in dynamics. Weaker vortices will dissipate energy when they reach the interface and although a remnant of the vortex pair transits the interface, it does not achieve the same altitude that it would have without the interface. Overall, the interface is not a barrier to vortex pairs, but would be expected to change the distribution of energy in more complicated flows.

Introduction

The Earth's atmosphere is warmest at the ground on average, and becomes cooler with increasing altitude. This cooling trend continues with surprisingly constant rate (the lapse rate) until the tropopause altitude, approximately 12 km at mid-latitudes. Beyond the tropopause, the temperature *increases* with approximately constant rate. This sudden change in the sign of the gradient of temperature is important for internal waves and other dynamic processes. Two other persistent density gradient interfaces exist at higher altitudes: the stratopause at approximately 40 km and the mesopause at approximately 90 km. All of these interfaces are important to weather and climate. The tropopause is also important to civil and military airplane operation. Commercial airliners in particular often cruise at or near the tropopause altitude, and need to avoid strong turbulence that might exist there.

The buoyancy frequency is the maximum frequency of internal waves, and in a compressible atmosphere is defined as

$$N = \sqrt{\frac{g}{\bar{\theta}} \frac{d\bar{\theta}}{dz}},$$

where θ is the potential temperature, z is the vertical distance, g is the gravitational constant, and the overline indicates a mean quantity. The sudden change in the gradient of the mean temperature also has a corresponding change in the gradient of potential temperature, $\frac{d\bar{\theta}}{dz}$, and therefore a sudden change in N . The tropopause therefore is an altitude where internal waves must adjust to this sudden change in background state. It has been known for a long time that linear internal waves will reflect at the tropopause [14]. More recent work has shown that nonlinear internal waves will create a horizontal mean flow at the tropopause altitude [7] and that higher harmonics will accumulate at the tropopause [8], indicating that the tropopause is a location of strong nonlinear wave behavior, including breaking waves and the resulting turbulence that is created. Recent observations appear to

confirm that the tropopause may have higher levels of turbulence than that found at other altitudes [5, 13].

Density interfaces (as opposed to density-gradient interfaces) are well-known to restrict the dynamics of turbulence, sometimes even providing a barrier to the spreading of turbulence. Shear flows can also act as a turbulence guide. The ability of a density gradient interface to restrict turbulence is considered here using a vortex pair. A counter-rotating vortex pair in a stratified fluid is a common model of the trailing vortex system behind an airplane. This vortex system has often been treated with constant density flow. Saffman [12] included stratification without any interfaces using a relatively simple conceptual technique. Saffman recognized that mixing within the vortex pair will result in a uniform density within the vortex, making the vortex buoyant. As a result of the buoyancy, Saffman predicts that an ascending vortex pair will reach a maximum vertical position and then descend. However Saffman's results assumed that the vortices remain a fixed distance apart, something that is not in general true. More recently, Garten, Arendt, Fritts, and Werne [4] treated a vortex pair in a stratified fluid using direct numerical simulations again without interfaces. Garten et. al. showed that the important parameter is what they called the Froude number:

$$\overline{F}_r = \frac{W_0}{Nb_0},$$

where W_0 is the vortex strength and b_0 is the initial spacing of the vortices. Garten et. al. state that there are two categories of behavior for the vortex pair released in a stratified atmosphere. One outcome is that the vortex pair will very quickly dissipate into internal waves which propagate away from the location of the vortex pair. This happens when the initial vortices have \overline{F}_r less than unity which corresponds to relatively weak vortices. The second outcome is vertical propagation of a coherent vortex pair, which occurs when \overline{F}_r is greater than unity corresponding to relatively strong vortices. Garten, et. al. [4] also showed that the vortices move closer together during their evolution, causing much faster vertical motion of the pair.

The dynamics of a vortex pair in a stratified atmosphere near a density gradient interface is considered here using direct numerical simulations. The vortex pair is released below the

interface and allowed to propagate vertically toward the interface. The results show that strong vortices propagate through the interface without much change in dynamics. Weaker vortices will dissipate energy when they reach the interface and although a remnant of the vortex pair transits the interface, it does not achieve the same altitude that it would have without the interface. Overall, the interface is not a barrier to vortex pairs, but would be expected to change the distribution of energy in more complicated flows.

CHAPTER I

Governing Equations

The governing equations are the two-dimensional anelastic equations. The anelastic equations are the Navier Stokes equations with the effects due to sound wave propagation removed. For a two-dimensional compressible atmosphere, the anelastic equations are

$$\frac{\partial u}{\partial t} + u \frac{\partial u}{\partial x} + w \frac{\partial u}{\partial z} = -\frac{\partial p^*}{\partial x} + \nu \left[\frac{\partial^2 u}{\partial x^2} + \frac{\partial^2 u}{\partial z^2} \right], \quad (\text{I.1})$$

$$\frac{\partial w}{\partial t} + u \frac{\partial w}{\partial x} + w \frac{\partial w}{\partial z} = -\frac{\partial p^*}{\partial z} + g \frac{\theta}{\bar{\theta}} + \nu \left[\frac{\partial^2 w}{\partial x^2} + \frac{\partial^2 w}{\partial z^2} \right], \quad (\text{I.2})$$

$$\frac{\partial \theta}{\partial t} + u \frac{\partial \theta}{\partial x} + w \frac{\partial \theta}{\partial z} + w \frac{\partial \bar{\theta}}{\partial z} = \kappa \left[\frac{\partial^2 \theta}{\partial x^2} + \frac{\partial^2 \theta}{\partial z^2} \right], \quad (\text{I.3})$$

$$\frac{\partial \bar{\rho} u}{\partial x} + \frac{\partial \bar{\rho} w}{\partial z} = 0, \quad (\text{I.4})$$

$$p^* = c_p \bar{\theta} \left(\frac{p}{p_0} \right)^{\frac{R}{c_p}}, \quad (\text{I.5})$$

$$\theta = T \left(\frac{p_0}{\bar{p}} \right)^{\frac{R}{c_p}}, \quad (\text{I.6})$$

where the horizontal and vertical velocities are u and w , respectively, the horizontal and vertical components of position are x and z , respectively, the potential temperature is θ , the pressure is p , the temperature is T , the specific heat at constant pressure is c_p , the gas constant is R , the kinematic viscosity is ν , the thermal diffusivity is κ and p_0 is a constant. The background state is indicated with an overbar: $\bar{\rho}$ and $\bar{\theta}$.

Re-Scaling

The horizontal length of the domain is L , and the vertical height is D . The coordinate system origin is chosen to be at the bottom left corner of the domain, thus $0 \leq x \leq L$ and $0 \leq z \leq D$.

The equations will be treated using a spectral method, with a periodic horizontal direction, and a non-periodic vertical direction. The horizontal direction is treated using Fourier series while the vertical direction uses Chebyshev-Gauss-Lobatto collocation.

This choice of basis function requires the horizontal computational domain to be $0 \leq \tilde{x} \leq 2\pi$ and the vertical computational domain to be $-1 \leq \tilde{z} \leq 1$, shown in Figure I.1. The domain is rescaled using

$$\frac{x}{L} = \frac{\tilde{x}}{2\pi}, \quad \text{and} \quad \frac{z}{D} = \frac{\tilde{z} + 1}{2}. \quad (\text{I.7})$$

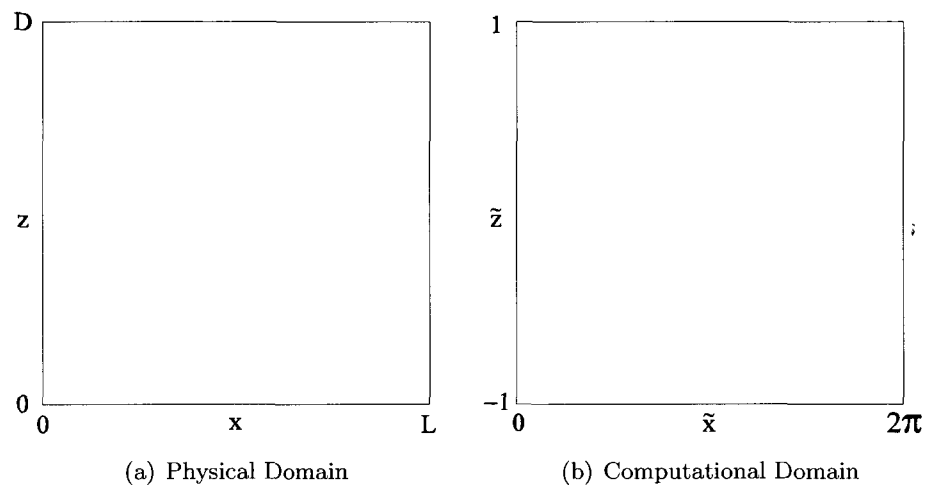


Figure I.1: The dimensional physical domain and the computational domain after rescaling.

The other variables are non-dimensionalized using

$$u = U\tilde{u}, \quad w = U\tilde{w}, \quad (\text{I.8})$$

$$t = \frac{L}{2\pi U}\tilde{t}, \quad (\text{I.9})$$

$$\theta = \bar{\theta}_0\tilde{\theta}, \quad (\text{I.10})$$

$$p^* = U^2\tilde{p}^*, \quad (\text{I.11})$$

where U is a velocity scale and $\bar{\theta}_0$ is a constant.

The rescaled dimensionless equations are

$$\frac{\partial\tilde{u}}{\partial\tilde{x}} + \frac{z_{sc}}{\tilde{\rho}}\frac{\partial\tilde{\rho}}{\partial\tilde{z}}\tilde{w} + z_{sc}\frac{\partial\tilde{w}}{\partial\tilde{z}} = 0, \quad (\text{I.12})$$

$$\frac{\partial\tilde{u}}{\partial\tilde{t}} + \tilde{u}\frac{\partial\tilde{u}}{\partial\tilde{x}} + z_{sc}\tilde{w}\frac{\partial\tilde{u}}{\partial\tilde{z}} = -\frac{\partial\tilde{p}^*}{\partial\tilde{x}} + \frac{2\pi}{Re}\left[\left(\frac{\partial^2\tilde{u}}{\partial\tilde{x}^2} + z_{sc}^2\frac{\partial^2\tilde{u}}{\partial\tilde{z}^2}\right)\right], \quad (\text{I.13})$$

$$\frac{\partial\tilde{w}}{\partial\tilde{t}} + \tilde{u}\frac{\partial\tilde{w}}{\partial\tilde{x}} + z_{sc}\tilde{w}\frac{\partial\tilde{w}}{\partial\tilde{z}} = -z_{sc}\frac{\partial\tilde{p}^*}{\partial\tilde{z}} + \frac{1}{2\pi Fr_r^2}\frac{\tilde{\theta}}{\tilde{\theta}} + \frac{2\pi}{Re}\left[\frac{\partial^2\tilde{w}}{\partial\tilde{x}^2} + z_{sc}^2\frac{\partial^2\tilde{w}}{\partial\tilde{z}^2}\right], \quad (\text{I.14})$$

$$\frac{\partial\tilde{\theta}}{\partial\tilde{t}} + \tilde{u}\frac{\partial\tilde{\theta}}{\partial\tilde{x}} + \tilde{w}z_{sc}\frac{\partial\tilde{\theta}}{\partial\tilde{z}} + \tilde{w}z_{sc}\frac{\partial\tilde{\theta}}{\partial\tilde{z}} = \frac{2\pi}{RePr}\left[\frac{\partial^2\tilde{\theta}}{\partial\tilde{x}^2} + z_{sc}^2\frac{\partial^2\tilde{\theta}}{\partial\tilde{z}^2}\right], \quad (\text{I.15})$$

where,

$$z_{sc} = \frac{L}{\pi D}. \quad (\text{I.16})$$

The Reynolds, Froude and Prandtl numbers are

$$Re = \frac{UL}{\nu}, \quad Fr^2 = \frac{U^2}{gL}, \quad Pr = \frac{\nu}{\kappa}. \quad (\text{I.17})$$

The side boundaries are periodic, and do not require additional enforcement of boundary conditions. The top and bottom boundaries are no-slip and have zero potential temperature fluctuation:

$$\tilde{u} \Big|_{\tilde{z}=-1,1} = \tilde{w} \Big|_{\tilde{z}=-1,1} = \tilde{\theta} \Big|_{\tilde{z}=-1,1} = 0. \quad (\text{I.18})$$

These boundary conditions allow for the reflection of waves back into the computational domain. The maximum vertical speed of an internal wave created at the same location as the vortex pair would reflect off the bottom and reach the vortex in $\tilde{t} = 23$. However, these waves have a very low energy value and the associated effects are considered negligible.

CHAPTER II

Background State

The two basic state quantities that are needed are $\bar{\theta}$ and $\bar{\rho}$. Three equations are required to fully define the basic state : the perfect gas law,

$$\bar{p} = \bar{\rho}R\bar{T}, \quad (\text{II.1})$$

the equation of static equilibrium,

$$\frac{\partial \bar{p}}{\partial z} = -\bar{\rho}g, \quad (\text{II.2})$$

and the definition of potential temperature,

$$\bar{\theta} = \bar{T} \left(\frac{p_0}{\bar{p}} \right)^{\frac{R}{c_p}}. \quad (\text{II.3})$$

Single Layer

Typically the base state temperature is first chosen and the other base state variables are then calculated. To obtain the base state density, eliminate pressure between (II.1) and (II.2):

$$\frac{\partial}{\partial z} [\bar{\rho}R\bar{T}] = -\bar{\rho}g. \quad (\text{II.4})$$

Separate the variables, and integrate:

$$\bar{\rho} = C_1 e^{-\int_0^z \left[\frac{g+R\frac{\partial \bar{T}}{\partial z}}{R\bar{T}} \right] dz}. \quad (\text{II.5})$$

The value of the background density at the bottom of the domain is ρ_0 ; thus,

$$\begin{aligned} \tilde{\rho} &= \frac{\bar{\rho}_0}{\rho_0} e^{\frac{\tilde{N}_0^2}{L} \frac{D}{2} (\tilde{z}+1)} \\ &= e^{\frac{\tilde{N}_0^2}{2\pi} \frac{\pi D}{L} (\tilde{z}+1)} \end{aligned} \quad (\text{II.6})$$

$$\tilde{\rho} = e^{\frac{\tilde{N}_0^2}{2\pi z_{sc}} (\tilde{z}+1)}. \quad (\text{II.7})$$

The potential temperature and pressure can be found using (II.1) and (II.3). Two important quantities are the Brunt-Vaisala frequency, N , and the scale height, H :

$$N^2 = g \frac{\bar{\theta}_z}{\bar{\theta}}, \quad (\text{II.8})$$

$$\frac{1}{H} = -\frac{\bar{\rho}_z}{\bar{\rho}}. \quad (\text{II.9})$$

Equations (II.1), (II.2) and (II.3) are manipulated to create two convenient relations. Combine the perfect gas law and the equation for static equilibrium to obtain

$$\frac{\bar{\rho}_z}{\bar{\rho}} + \frac{\bar{T}_z}{\bar{T}} + \frac{g}{R\bar{T}} = 0. \quad (\text{II.10})$$

The second relation uses the definition of potential temperature along with the other two equations:

$$\frac{\bar{T}_z}{\bar{T}} + \frac{g}{c_p \bar{T}} - \frac{\bar{\theta}_z}{\bar{\theta}} = 0. \quad (\text{II.11})$$

If the background temperature is chosen to be constant, then

$$\frac{\partial \bar{T}}{\partial z} = 0. \quad (\text{II.12})$$

Equations (II.10) and (II.11) reduce to

$$\frac{\bar{\rho}_z}{\bar{\rho}} + \frac{g}{R\bar{T}} = 0, \quad (\text{II.13})$$

and

$$\frac{g}{c_p \bar{T}} - \frac{\bar{\theta}_z}{\bar{\theta}} = 0. \quad (\text{II.14})$$

Equation (II.14) relates the background temperature to the Brunt-Vaisala frequency:

$$\bar{T} = \frac{g^2}{c_p N^2}. \quad (\text{II.15})$$

Thus, constant temperature means constant Brunt-Vaisala frequency. The base state potential temperature profile is determined by separating the variables in (II.14) and integrating:

$$\bar{\theta} = \bar{\theta}_0 e^{\frac{g}{c_p \bar{T}} z} = \bar{\theta}_0 e^{\frac{N^2}{g} z}. \quad (\text{II.16})$$

Rescale the Brunt-Vaisala frequency as before:

$$N^2 = \frac{U^2}{L^2} \tilde{N}_0^2. \quad (\text{II.17})$$

The rescaled background potential temperature is

$$\tilde{\theta} = e^{\frac{F_r^2 \tilde{N}_0^2}{2\pi z s c} (\tilde{z}+1)}. \quad (\text{II.18})$$

The mean flow is zero in the results given below. Therefore, another definition for U must

be chosen: $U = \sqrt{gL}$. The Froude number then reduces to unity:

$$F_r^2 = 1. \quad (\text{II.19})$$

The rescaled Brunt-Vaisala frequency is modified slightly:

$$N^2 = \frac{g}{L} \tilde{N}_0^2. \quad (\text{II.20})$$

By (II.13), since \bar{T} is a constant, $\frac{\bar{\rho}_z}{\bar{\rho}}$ is also constant, as is the scale height:

$$\frac{1}{H} = -\frac{\bar{\rho}_z}{\bar{\rho}} = \frac{g}{R\bar{T}}. \quad (\text{II.21})$$

A new parameter is introduced here purely for notation convenience:

$$\hat{N}^2 = -\frac{1}{H} = -\frac{g}{R\bar{T}} = \frac{\bar{\rho}_z}{\bar{\rho}} \quad (\text{II.22})$$

Rescale \hat{N} :

$$\hat{N}^2 = \frac{\tilde{N}_0^2}{L}, \quad (\text{II.23})$$

and the background density,

$$\tilde{\rho} = e^{\frac{\tilde{N}_0^2}{2\pi z_{sc}}(\tilde{z}+1)}. \quad (\text{II.24})$$

Two Layer

A two-layer base state is chosen with each layer having a constant and unique value of \bar{T} .

The resulting Brunt-Vaisala frequencies and scale heights are

$$N_1^2 = \frac{g^2}{c_{p1}\bar{T}_1}, \quad (\text{II.25})$$

$$N_2^2 = \frac{g^2}{c_{p2}\bar{T}_2}, \quad (\text{II.26})$$

$$\frac{1}{H_1} = \frac{g}{R_1\bar{T}_1}, \quad (\text{II.27})$$

$$\frac{1}{H_2} = \frac{g}{R_2\bar{T}_2}, \quad (\text{II.28})$$

where subscript ‘1’ indicates the lower layer, and ‘2’ denotes the upper layer. At the interface the pressure of the lower layer must match that of the upper layer:

$$\bar{p}_1 \Big|_{z=z_a} = \bar{p}_2 \Big|_{z=z_a}, \quad (\text{II.29})$$

where z_a is the height of the interface. Since the density is continuous across the interface, the perfect gas law and (II.29) results in

$$R_1\bar{T}_1 = R_2\bar{T}_2. \quad (\text{II.30})$$

As a result, scale heights in the two layers are equal:

$$\frac{1}{H_1} = \frac{g}{R_1\bar{T}_1} = \frac{g}{R_2\bar{T}_2} = \frac{1}{H_2}, \quad (\text{II.31})$$

thus,

$$H_1 = H_2. \quad (\text{II.32})$$

In addition to pressure and density being continuous along the interface the potential temperature is chosen to be continuous at the layer interface. The potential temperature in each layer is,

$$\bar{\theta}_1 = \bar{\theta}_0 e^{\frac{N_1^2}{g}z}, \quad (\text{II.33})$$

and

$$\bar{\theta}_2 = \bar{\theta}_a e^{\frac{N_2^2}{g} z}. \quad (\text{II.34})$$

Equating $\bar{\theta}_1$ to $\bar{\theta}_2$ at the interface, ($z = z_a$), determines $\bar{\theta}_a$:

$$\bar{\theta}_a = \bar{\theta}_0 e^{\frac{N_2^2 - N_1^2}{g} z_a}. \quad (\text{II.35})$$

Rescale as before to obtain

$$\frac{\tilde{\theta}_1}{\bar{\theta}_0} = \frac{\bar{\theta}_1}{\bar{\theta}_0} = e^{\frac{N_1^2}{g} z} = e^{\frac{F_r^2 \tilde{N}_0^2}{2\pi z_{sc}} (\tilde{z}+1)} \quad (\text{II.36})$$

where

$$N_1^2 = \frac{U^2}{L^2} \tilde{N}_0^2. \quad (\text{II.37})$$

For the top layer,

$$\frac{\tilde{\theta}_2}{\bar{\theta}_0} = \frac{\bar{\theta}_2}{\bar{\theta}_0} = \frac{\bar{\theta}_a}{\bar{\theta}_0} e^{\frac{N_2^2}{g} z} = \frac{\bar{\theta}_a}{\bar{\theta}_0} e^{\frac{N_2^2 - N_1^2}{g} z} = \frac{\bar{\theta}_a}{\bar{\theta}_0} e^{\frac{F_r^2 \frac{N_2^2}{N_1^2} \tilde{N}_0^2}{2\pi z_{sc}} (\tilde{z}+1)} \quad (\text{II.38})$$

The value $\frac{N_2^2}{N_1^2}$ is chosen to be 4 for all results.

CHAPTER III

Computational Method

The computational method for temporal integration is that of Slinn and Riley [2]. The method uses four steps, three for the horizontal and vertical flow and one for the potential temperature. The first step solves explicitly for an auxiliary flow field, the second step determines the pressure field, and the last step combines the pressure field and the auxiliary flow to determine the final velocity field. The solution of the potential temperature profile is performed explicitly.

Consider the horizontal component of the Navier-Stokes equation:

$$\frac{\partial \tilde{u}}{\partial \tilde{t}} + \tilde{u} \frac{\partial \tilde{u}}{\partial \tilde{x}} + z_{sc} \tilde{w} \frac{\partial \tilde{u}}{\partial \tilde{x}} = -\frac{\partial \tilde{p}^*}{\partial \tilde{x}} + \frac{2\pi}{R_e} \left[\frac{\partial^2 \tilde{u}}{\partial \tilde{x}^2} + z_{sc}^2 \frac{\partial^2 \tilde{u}}{\partial \tilde{z}^2} \right]. \quad (\text{III.1})$$

The auxiliary horizontal velocity, u^* , is defined by

$$\frac{\partial \tilde{u}^*}{\partial \tilde{t}} = \frac{\partial \tilde{u}}{\partial \tilde{t}} + \frac{\partial \tilde{p}^*}{\partial \tilde{x}}. \quad (\text{III.2})$$

Inserting this into (III.1) gives

$$\frac{\partial \tilde{u}^*}{\partial \tilde{t}} = -\tilde{u} \frac{\partial \tilde{u}}{\partial \tilde{x}} - z_{sc} \tilde{w} \frac{\partial \tilde{u}}{\partial \tilde{x}} + \frac{2\pi}{R_e} \left[\frac{\partial^2 \tilde{u}}{\partial \tilde{x}^2} + z_{sc}^2 \frac{\partial^2 \tilde{u}}{\partial \tilde{z}^2} \right]. \quad (\text{III.3})$$

Discretizing in time using third order Adams-Bashforth,

$$\begin{aligned} \frac{\partial \tilde{u}^*}{\partial \tilde{t}} = \frac{\tilde{u}^* - \tilde{u}^n}{\Delta t} &= \frac{23}{16} \left[-\tilde{u} \frac{\partial \tilde{u}}{\partial \tilde{x}} - \tilde{w} \frac{\partial \tilde{u}}{\partial \tilde{z}} + \frac{2\pi}{R_e} \left(\frac{\partial^2 \tilde{u}}{\partial \tilde{x}^2} + \frac{\partial^2 \tilde{u}}{\partial \tilde{z}^2} \right) \right]^n \\ &\quad - \frac{12}{16} \left[-\tilde{u} \frac{\partial \tilde{u}}{\partial \tilde{x}} - \tilde{w} \frac{\partial \tilde{u}}{\partial \tilde{z}} + \frac{2\pi}{R_e} \left(\frac{\partial^2 \tilde{u}}{\partial \tilde{x}^2} + \frac{\partial^2 \tilde{u}}{\partial \tilde{z}^2} \right) \right]^{n-1} \\ &\quad + \frac{5}{16} \left[-\tilde{u} \frac{\partial \tilde{u}}{\partial \tilde{x}} - \tilde{w} \frac{\partial \tilde{u}}{\partial \tilde{z}} + \frac{2\pi}{R_e} \left(\frac{\partial^2 \tilde{u}}{\partial \tilde{x}^2} + \frac{\partial^2 \tilde{u}}{\partial \tilde{z}^2} \right) \right]^{n-2}. \end{aligned} \quad (\text{III.4})$$

The same procedure is performed with the vertical component. The auxiliary vertical velocity, w^* is defined by

$$\frac{\partial \tilde{w}^*}{\partial \tilde{t}} = \frac{\partial \tilde{w}}{\partial \tilde{t}} + z_{sc} \frac{\partial \tilde{p}^*}{\partial \tilde{z}}, \quad (\text{III.5})$$

and when inserted into (I.14), results in

$$\begin{aligned} \frac{\tilde{w}^* - \tilde{w}^n}{\Delta t} &= \frac{23}{16} \left[-\tilde{u} \frac{\partial \tilde{w}}{\partial \tilde{x}} - \tilde{w} \frac{\partial \tilde{w}}{\partial \tilde{z}} + \frac{1}{2\pi F_r^2} \frac{\tilde{\theta}}{\tilde{\theta}} + \frac{2\pi}{R_e} \left(\frac{\partial^2 \tilde{w}}{\partial \tilde{x}^2} + \frac{\partial^2 \tilde{w}}{\partial \tilde{z}^2} \right) \right]^n \\ &\quad - \frac{12}{16} \left[-\tilde{u} \frac{\partial \tilde{w}}{\partial \tilde{x}} - \tilde{w} \frac{\partial \tilde{w}}{\partial \tilde{z}} + \frac{1}{2\pi F_r^2} \frac{\tilde{\theta}}{\tilde{\theta}} + \frac{2\pi}{R_e} \left(\frac{\partial^2 \tilde{w}}{\partial \tilde{x}^2} + \frac{\partial^2 \tilde{w}}{\partial \tilde{z}^2} \right) \right]^{n-1} \\ &\quad + \frac{5}{16} \left[-\tilde{u} \frac{\partial \tilde{w}}{\partial \tilde{x}} - \tilde{w} \frac{\partial \tilde{w}}{\partial \tilde{z}} + \frac{1}{2\pi F_r^2} \frac{\tilde{\theta}}{\tilde{\theta}} + \frac{2\pi}{R_e} \left(\frac{\partial^2 \tilde{w}}{\partial \tilde{x}^2} + \frac{\partial^2 \tilde{w}}{\partial \tilde{z}^2} \right) \right]^{n-2}. \end{aligned} \quad (\text{III.6})$$

Note that u^* and w^* do not necessarily conform to continuity.

Now solve for \tilde{p}^* using the values of the auxiliary flow fields and the conservation of mass. Integrate (III.2) over a single time step,

$$\frac{\partial \tilde{u}^*}{\partial \tilde{t}} = \frac{\partial \tilde{u}}{\partial \tilde{t}} + \frac{\partial \tilde{p}^*}{\partial \tilde{x}} \quad (\text{III.7})$$

$$\frac{\tilde{u}^* - \tilde{u}^n}{\Delta t} = \frac{\tilde{u}^{n+1} - \tilde{u}^n}{\Delta t} + \frac{\partial \tilde{p}^*}{\partial \tilde{x}} \quad (\text{III.8})$$

and take a horizontal derivative to obtain

$$\frac{\partial \tilde{u}^{n+1}}{\partial \tilde{x}} = \frac{\partial \tilde{u}^*}{\partial \tilde{x}} - \Delta t \frac{\partial^2 \tilde{p}^*}{\partial \tilde{x}^2}. \quad (\text{III.9})$$

Integrate (III.5) similarly,

$$\frac{\tilde{w}^* - \tilde{w}^n}{\Delta t} = \frac{\tilde{w}^{n+1} - \tilde{w}^n}{\Delta t} + z_{sc} \frac{\partial \tilde{p}^*}{\partial \tilde{z}}, \quad (\text{III.10})$$

then take a vertical derivative:

$$z_{sc} \frac{\partial \tilde{w}^{n+1}}{\partial \tilde{z}} + z_{sc} \frac{\tilde{w}^{n+1}}{\tilde{\rho}} \frac{\partial \tilde{\rho}}{\partial \tilde{z}} = z_{sc} \frac{\partial \tilde{w}^*}{\partial \tilde{z}} + z_{sc} \frac{\tilde{w}^*}{\tilde{\rho}} \frac{\partial \tilde{\rho}}{\partial \tilde{z}} - \Delta t z_{sc}^2 \frac{\partial^2 \tilde{p}^*}{\partial \tilde{z}^2} - \Delta t z_{sc}^2 \frac{1}{\tilde{\rho}} \frac{\partial \tilde{\rho}}{\partial \tilde{z}} \frac{\partial \tilde{p}^*}{\partial \tilde{z}}. \quad (\text{III.11})$$

Add (III.9) and (III.9) to obtain

$$\frac{1}{\Delta t} \left[\frac{\partial \tilde{u}^*}{\partial \tilde{x}} + z_{sc} \frac{\tilde{w}^*}{\tilde{\rho}} \frac{\partial \tilde{\rho}}{\partial \tilde{z}} + z_{sc} \frac{\partial \tilde{w}^*}{\partial \tilde{z}} \right] = \frac{\partial^2 \tilde{p}^*}{\partial \tilde{x}^2} + \frac{z_{sc}^2}{\tilde{\rho}} \frac{\partial \tilde{p}^*}{\partial \tilde{z}} \frac{\partial \tilde{\rho}}{\partial \tilde{z}} + z_{sc}^2 \frac{\partial \tilde{p}^*}{\partial \tilde{z}}. \quad (\text{III.12})$$

The boundary condition on pressure used in the simulation is

$$\frac{\partial \tilde{p}^*}{\partial \tilde{z}} = - \frac{\tilde{w}^*}{z_{sc} \Delta t}. \quad (\text{III.13})$$

From (III.13) it may appear an infinite change in pressure is expressed as the time step is decreased. However, \tilde{w}^* also goes to zero on the boundary with Δt , and the right-hand-side of (III.13) remains finite. More sophisticated methods can be used for the pressure boundary. However, for large Re this proves unnecessary [11]. This can also be seen by expressing $\frac{\partial \tilde{p}^*}{\partial \tilde{z}}$ in terms of \tilde{w} rather than \tilde{w}^* :

$$\frac{\partial \tilde{p}^*}{\partial \tilde{z}} = \frac{2\pi}{z_{sc} Re} \left[\frac{23}{16} \frac{\partial^2 \tilde{w}^n}{\partial \tilde{z}^2} - \frac{12}{16} \frac{\partial^2 \tilde{w}^{n-1}}{\partial \tilde{z}^2} + \frac{5}{16} \frac{\partial^2 \tilde{w}^{n-2}}{\partial \tilde{z}^2} \right]. \quad (\text{III.14})$$

Note that Δt no longer appears in the denominator of this expression.

The final step finds \tilde{u}^{n+1} and \tilde{w}^{n+1} using (III.8) and (III.10): \tilde{u}^* and \tilde{w}^* ,

$$\tilde{u}^{n+1} = \tilde{u}^* - \Delta t \frac{\partial \tilde{p}^*}{\partial \tilde{x}} \quad (\text{III.15})$$

and

$$\tilde{w}^{n+1} = \tilde{w}^* - z_{sc} \Delta t \frac{\partial \tilde{p}^*}{\partial \tilde{x}}. \quad (\text{III.16})$$

Integrate (I.15) using the same third order Adams-Bashforth method to get,

$$\begin{aligned}
\frac{\tilde{\theta}^{n+1} - \tilde{\theta}^n}{\Delta t} &= \frac{23}{16} \left[-\tilde{u} \frac{\partial \tilde{\theta}}{\partial \tilde{x}} - \tilde{w} \frac{\partial \tilde{\theta}}{\partial \tilde{z}} - \tilde{w} \frac{\partial \tilde{\theta}}{\partial \tilde{z}} + \frac{2\pi}{R_e P_r} \left(\frac{\partial^2 \tilde{\theta}}{\partial \tilde{x}^2} + \frac{\partial^2 \tilde{\theta}}{\partial \tilde{z}^2} \right) \right]^n \\
&\quad - \frac{12}{16} \left[-\tilde{u} \frac{\partial \tilde{\theta}}{\partial \tilde{x}} - \tilde{w} \frac{\partial \tilde{\theta}}{\partial \tilde{z}} - \tilde{w} \frac{\partial \tilde{\theta}}{\partial \tilde{z}} + \frac{2\pi}{R_e P_r} \left(\frac{\partial^2 \tilde{\theta}}{\partial \tilde{x}^2} + \frac{\partial^2 \tilde{\theta}}{\partial \tilde{z}^2} \right) \right]^{n-1} \\
&\quad + \frac{5}{16} \left[-\tilde{u} \frac{\partial \tilde{\theta}}{\partial \tilde{x}} - \tilde{w} \frac{\partial \tilde{\theta}}{\partial \tilde{z}} - \tilde{w} \frac{\partial \tilde{\theta}}{\partial \tilde{z}} + \frac{2\pi}{R_e P_r} \left(\frac{\partial^2 \tilde{\theta}}{\partial \tilde{x}^2} + \frac{\partial^2 \tilde{\theta}}{\partial \tilde{z}^2} \right) \right]^{n-2}.
\end{aligned} \tag{III.17}$$

The computational domain is discretized spatially using a Fourier transform in the horizontal and Chebyshev-Gauss-Lobatto collocation in the vertical. Discrete Fourier series [1] for N_x terms are

$$\hat{u}_n = \frac{1}{N_x} \sum_{j=0}^{N_x-1} u_j e^{-i2\pi nj/N_x}. \tag{III.18}$$

The vertical direction uses collocation on the Chebyshev-Gauss-Lobatto points:

$$z_k = \cos \left(\frac{\pi k}{N_z} \right) \quad k = 0, N_z \tag{III.19}$$

where N_z is the resolution in the vertical direction. Vertical derivatives are performed by multiplication of a derivative matrix [1][6][15]. The derivative matrix is defined as

$$\left. \frac{dC_j}{dx} \right|_{x=x_i} = \begin{cases} \frac{1+2N_k^2}{6} & i = j = 0 \\ -\frac{1+2N_k^2}{6} & i = j = N_k \\ -\frac{x_j}{2(1-x_j^2)} & i = j; 0 < j < N_k \\ (-1)^{i+j} \frac{p_i}{p_j(x_i-x_j)} & i \neq j \end{cases} \tag{III.20}$$

CHAPTER IV

Initial Conditions

Single Vortex

The primary goal is to initiate two counter-rotating vortices and determine their behavior in a stratified flow. The initial conditions are chosen to be a diffusing line vortex, which is an exact solution to the constant-density viscous Navier-Stokes equations. The velocity field for a single vortex located at the origin in cylindrical coordinates is

$$u_\theta = \frac{\Gamma}{2\pi r} \left[1 - e^{-\frac{r^2}{2\nu t}} \right], \quad (\text{IV.1})$$

and

$$u_r = 0, \quad (\text{IV.2})$$

where u_r and u_θ are the azimuthal and radial velocity components, r is the radial distance, and Γ is the circulation.[3]

Convert to Cartesian coordinates using

$$u = u_r \cos \theta - u_\theta \sin \theta, \quad (\text{IV.3})$$

$$w = u_r \sin \theta + u_\theta \cos \theta, \quad (\text{IV.4})$$

and

$$\cos \theta = \frac{x}{\sqrt{x^2 + z^2}}, \quad (\text{IV.5})$$

$$\sin \theta = \frac{z}{\sqrt{x^2 + z^2}}. \quad (\text{IV.6})$$

The result is

$$u = -\frac{\Gamma}{2\pi} \frac{z}{x^2 + z^2} \left[1 - e^{-\frac{x^2+z^2}{2\nu t}} \right], \quad (\text{IV.7})$$

and

$$w = \frac{\Gamma}{2\pi} \frac{x}{x^2 + z^2} \left[1 - e^{-\frac{x^2+z^2}{2\nu t}} \right]. \quad (\text{IV.8})$$

Rescale using

$$u = W_0 \hat{u}, \quad (\text{IV.9})$$

$$w = W_0 \hat{w}, \quad (\text{IV.10})$$

$$x = b_0 \hat{x}, \quad (\text{IV.11})$$

$$z = b_0 \hat{z}, \quad (\text{IV.12})$$

where W_0 and b_0 are chosen to match previous work done by Fritts [4], and will be defined later:

$$\hat{u} = -\frac{\Gamma}{2\pi b_0 W_0} \frac{\hat{z}}{\hat{x}^2 + \hat{z}^2} \left[1 - e^{-\frac{b_0^2}{4\nu t}(\hat{x}^2 + \hat{z}^2)} \right], \quad (\text{IV.13})$$

$$\hat{w} = \frac{\Gamma}{2\pi b_0 W_0} \frac{\hat{x}}{\hat{x}^2 + \hat{z}^2} \left[1 - e^{-\frac{b_0^2}{4\nu t}(\hat{x}^2 + \hat{z}^2)} \right]. \quad (\text{IV.14})$$

Define,

$$W_0 = \frac{\Gamma}{2\pi b_0}, \quad (\text{IV.15})$$

$$\sigma^2 = 2\nu t, \quad (\text{IV.16})$$

$$\sigma = b_0 \hat{\sigma}, \quad (\text{IV.17})$$

finally getting

$$\hat{u} = -\frac{\hat{z}}{\hat{x}^2 + \hat{z}^2} \left[1 - e^{-\frac{\hat{x}^2 + \hat{z}^2}{2\hat{\sigma}^2}} \right], \quad (\text{IV.18})$$

and

$$\hat{w} = \frac{\hat{x}}{\hat{x}^2 + \hat{z}^2} \left[1 - e^{-\frac{\hat{x}^2 + \hat{z}^2}{2\hat{\sigma}^2}} \right]. \quad (\text{IV.19})$$

Symmetric Vortex Pair

Now consider a symmetric vortex pair, as shown in IV.1. The quantity b_0 is now defined as the distance between the vortices, and W_0 is the velocity induced at the center of one vortex by the other.

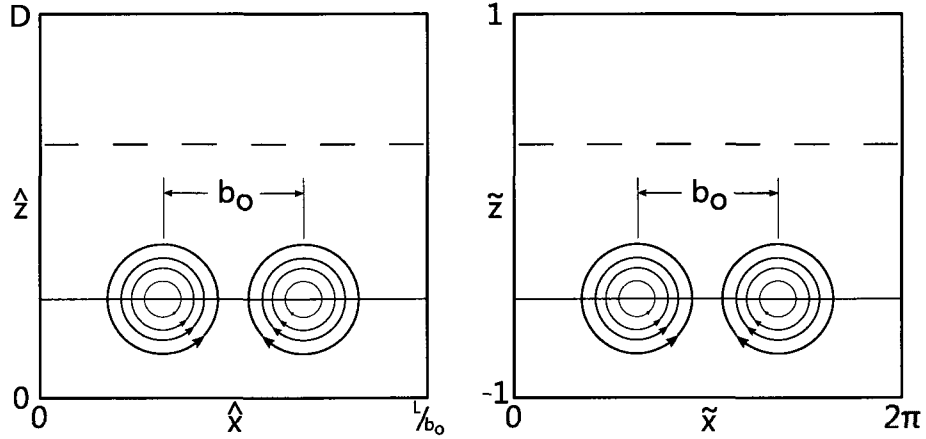


Figure IV.1: The initial conditions. The distance between the vortex centers is b_0 . The solid line is the release height and the dotted line is the interface height. The left figure is the physical domain with the right being representative of the domain after rescaling has occurred.

The left vortex has velocity components,

$$\hat{u}_1 = -\frac{\hat{z} - \hat{z}_1}{(\hat{x} - \hat{x}_1)^2 + (\hat{z} - \hat{z}_1)^2} \left[1 - e^{-\frac{(\hat{x} - \hat{x}_1)^2 + (\hat{z} - \hat{z}_1)^2}{2\hat{\sigma}^2}} \right] \quad (\text{IV.20})$$

and

$$\hat{w}_1 = \frac{\hat{x} - \hat{x}_1}{(\hat{x} - \hat{x}_1)^2 + (\hat{z} - \hat{z}_1)^2} \left[1 - e^{-\frac{(\hat{x} - \hat{x}_1)^2 + (\hat{z} - \hat{z}_1)^2}{2\hat{\sigma}^2}} \right], \quad (\text{IV.21})$$

where x_1 and z_1 are the location of the vortex center.

Although the quantities are all now dimensionless, they must be rescaled again to match the nondimensionalization of the governing equations:

$$\hat{x} = \frac{L}{2\pi b_0} \tilde{x}, \quad (\text{IV.22})$$

$$\hat{z} = \frac{D}{2b_0} (\tilde{z} + 1). \quad (\text{IV.23})$$

Define

$$b_{sc} = \frac{L}{2\pi b_0}. \quad (\text{IV.24})$$

Thus,

$$\hat{x} = b_{sc} \tilde{x}, \quad (\text{IV.25})$$

and

$$\hat{z} = \frac{b_{sc}}{z_{sc}} (\tilde{z} + 1). \quad (\text{IV.26})$$

Finally,

$$\tilde{u}_1 = -\frac{\tilde{z} - \tilde{z}_1}{b_{sc} z_{sc} [(\tilde{x} - \tilde{x}_1)^2 + \frac{1}{z_{sc}^2} (\tilde{z} - \tilde{z}_1)^2]} \left[1 - e^{-\frac{b_{sc}^2 [(\tilde{x} - \tilde{x}_1)^2 + \frac{1}{z_{sc}^2} (\tilde{z} - \tilde{z}_1)^2]}{2\hat{\sigma}^2}} \right] \left[\frac{1}{1 - e^{\frac{1}{2\hat{\sigma}^2}}} \right] \quad (\text{IV.27})$$

and

$$\tilde{w}_1 = \frac{\tilde{x} - \tilde{x}_1}{b_{sc}[(\tilde{x} - \tilde{x}_1)^2 + \frac{1}{z_{sc}^2}(\tilde{z} - \tilde{z}_1)^2]} \left[1 - e^{-\frac{b_{sc}^2[(\tilde{x} - \tilde{x}_1)^2 + \frac{1}{z_{sc}^2}(\tilde{z} - \tilde{z}_1)^2]}{2\sigma^2}} \right] \left[\frac{1}{1 - e^{\frac{1}{2\sigma^2}}} \right]. \quad (\text{IV.28})$$

The same procedure performed for the right-hand vortex results in

$$\tilde{u}_2 = -\frac{\tilde{z} - \tilde{z}_2}{b_{sc}z_{sc}[(\tilde{x} - \tilde{x}_2)^2 + \frac{1}{z_{sc}^2}(\tilde{z} - \tilde{z}_2)^2]} \left[1 - e^{-\frac{b_{sc}^2[(\tilde{x} - \tilde{x}_2)^2 + \frac{1}{z_{sc}^2}(\tilde{z} - \tilde{z}_2)^2]}{2\sigma^2}} \right] \left[\frac{1}{1 - e^{\frac{1}{2\sigma^2}}} \right] \quad (\text{IV.29})$$

and

$$\tilde{w}_2 = \frac{\tilde{x} - \tilde{x}_2}{b_{sc}[(\tilde{x} - \tilde{x}_2)^2 + \frac{1}{z_{sc}^2}(\tilde{z} - \tilde{z}_2)^2]} \left[1 - e^{-\frac{b_{sc}^2[(\tilde{x} - \tilde{x}_2)^2 + \frac{1}{z_{sc}^2}(\tilde{z} - \tilde{z}_2)^2]}{2\sigma^2}} \right] \left[\frac{1}{1 - e^{\frac{1}{2\sigma^2}}} \right]. \quad (\text{IV.30})$$

CHAPTER V

Results

The fundamental parameters are the Reynolds, Froude and Prandtl numbers:

$$Re = \frac{UL}{\nu} = \frac{\sqrt{gL^3}}{\nu}, \quad (\text{V.1})$$

$$Fr^2 = \frac{U^2}{gL} = \frac{\sqrt{gL^3}}{gL} = 1 \quad (\text{V.2})$$

and

$$Pr = \frac{\nu}{\kappa}. \quad (\text{V.3})$$

The Prandtl number was chosen to have a value of unity for all results, as this is a convenient approximation for the typical atmosphere value of 0.7. An additional parameter is the aspect ratio of the computational domain:

$$z_{sc} = \frac{L}{\pi D}. \quad (\text{V.4})$$

The initial conditions add two more parameters of importance, one related to the vortex strength,

$$G = \frac{\Gamma}{\sqrt{gL^3}}, \quad (\text{V.5})$$

and another relating to the spacing between vortices,

$$b_{sc} = \frac{L}{2\pi b_0}. \quad (\text{V.6})$$

For all results given here, the Reynolds number was chosen to have a constant value of 1,000,000. Similarly, the core size of the initial vortex was kept constant, and only the initial strength was changed between cases. All test results were performed in a square computational domain with $z_{sc} = \frac{1}{\pi}$. The domain size was chosen to model a 10 *km* by 10 *km* physical domain.

Single Layer

Garten, et. al., [4] treated the dynamics of a counter-rotating vortex pair in a single layer of stratified fluid with constant N , as discussed previously. The Froude number of Garten, et. al. [4],

$$\bar{F}_r = \frac{W_o}{N b_0}, \quad (\text{V.7})$$

will be referred to here as the alternate Froude number and is related to the fundamental parameters used here by

$$\bar{F}_r = \frac{2\pi G b_{sc}^2}{\tilde{N}}. \quad (\text{V.8})$$

For the purpose of validation, several cases considered by Garten, Arendt, Fritts and Werne [4] have been repeated using the present methods. The results of a typical case are shown in figure V.1 using shaded contours of vorticity. The parameters for this case are given in table V.1, and with $\bar{F}_r = 2$, this vortex pair exhibits vertical propagation of the vortex pair.

The present results match the previous results of Garten, et. al. [4] very well (see figure 1 of Garten, et. al.). The difference between the contours in figure V.1 and the contours in figure 1 of Garten, et. al. can be attributed mostly to the choice of contour values. The overall behavior of the vortex pair is the same.

Present Results	Garten, Arendt, Fritts and Werne
$F_r = 1$	$\bar{F}_r = 2$
$R_e = 1,000,000$	$\bar{R}_e = 1000$
$G = 0.028$	$G = 0.028$
$Res = 256 \times 256$	$Res = 512 \times 1536$

Table V.1: Input parameters from comparison to Garten, et. al. results

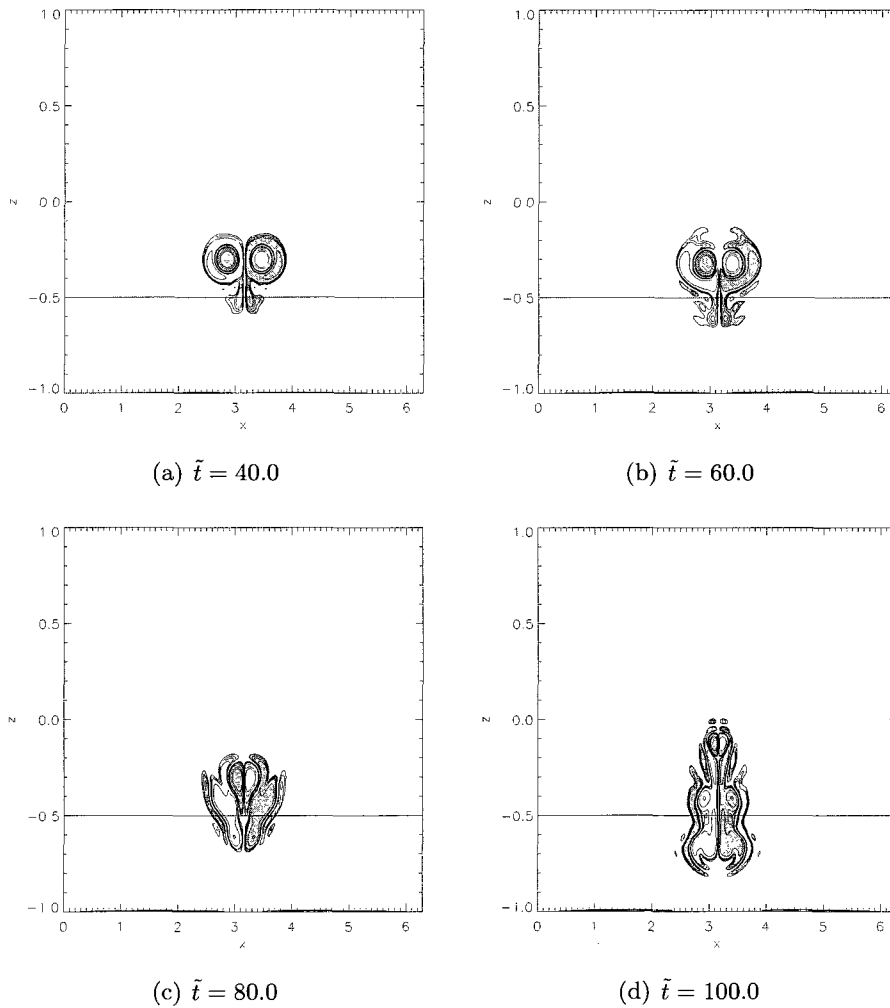


Figure V.1: Contours of vorticity from the results used for comparison with Garten, et. al.

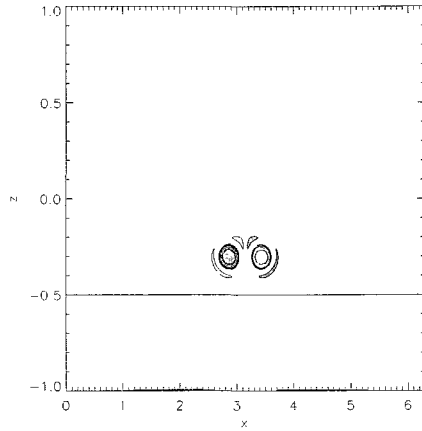
Numerical solution of the flow in a discrete vortex is well-known to be sensitive to spatial resolution. Simulations using the present methods with different resolutions have shown that a resolution of $N_x = 512$ and $N_z = 512$ (512×512) is adequate to resolve the flow throughout the life span of the vortices. However, this high resolution case is computationally expensive, taking four weeks on a recent desktop computer dedicated to the task. A lower resolution case (256×256) takes only several days on this same computer, and produces results with most of the same details. Note that the higher resolution case uses a smaller time step to avoid instability, exacerbating the problem.

Two simulations with identical parameters but different resolutions have been performed for a direct comparison. Figure V.2 shows shaded contours of vorticity for the high resolution case (512×512) while figure V.3 shows the same graphics for the low resolution case. A higher alternate Froude number was chosen ($\overline{F}_r = 4$) for this test so that the vortex pair would move further for a chosen time. Other parameter values are given in table V.2.

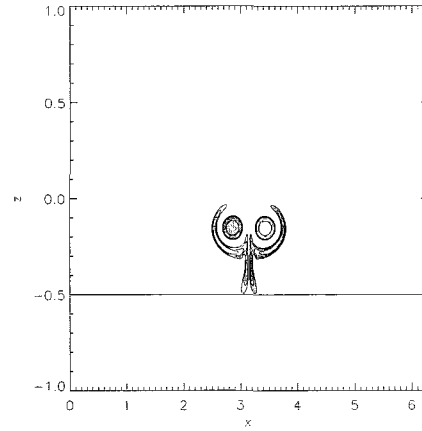
$\overline{F}_r = 4$ High Resolution Parameters
$F_r = 1$
$Re = 1,000,000$
$G = 0.056$
$Res = 256 \times 256$

Table V.2: $\overline{F}_r = 4$ High resolution parameter table

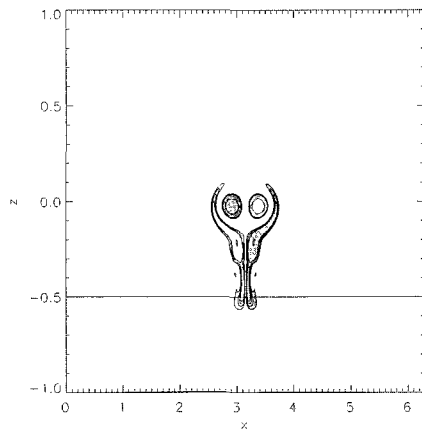
Figures V.2 and V.3 show that the vortex behavior is very similar with the different resolutions. The most visible differences are in the trailing wake beneath the vortex pair, which is unlikely to effect the vortex pair significantly. For practical reasons, most of the cases considered here have been treated with the lower resolution (256×256), with several cases at the higher resolution (512×512) to confirm conclusions.



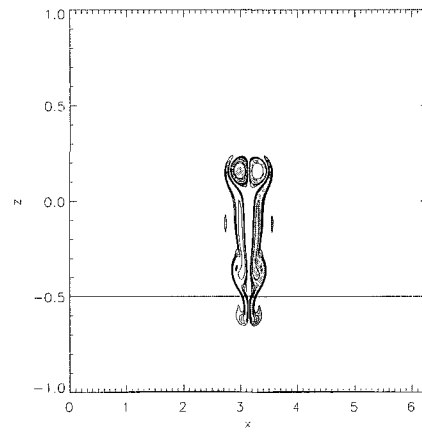
(a) $\bar{t} = 12.5$



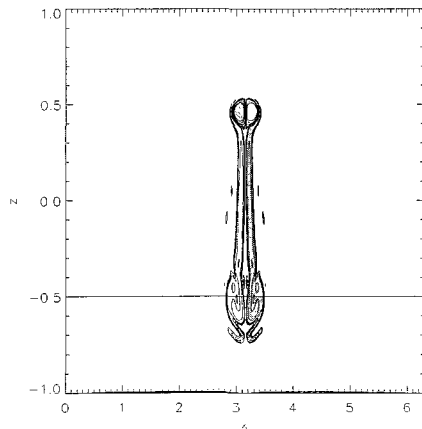
(b) $\bar{t} = 25.0$



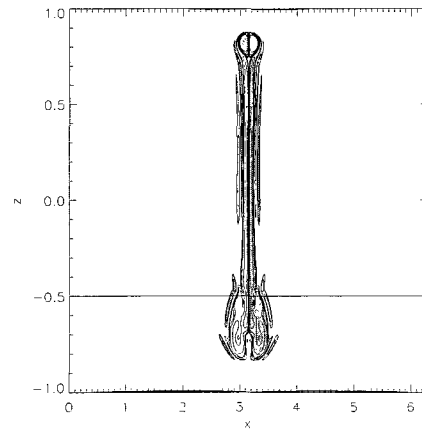
(c) $\bar{t} = 37.5$



(d) $\bar{t} = 50.0$



(e) $\bar{t} = 67.5$



(f) $\bar{t} = 75.0$

Figure V.2: Contours of vorticity for the single layer case with $\bar{F}_r = 4$ and a resolution of 512x512.

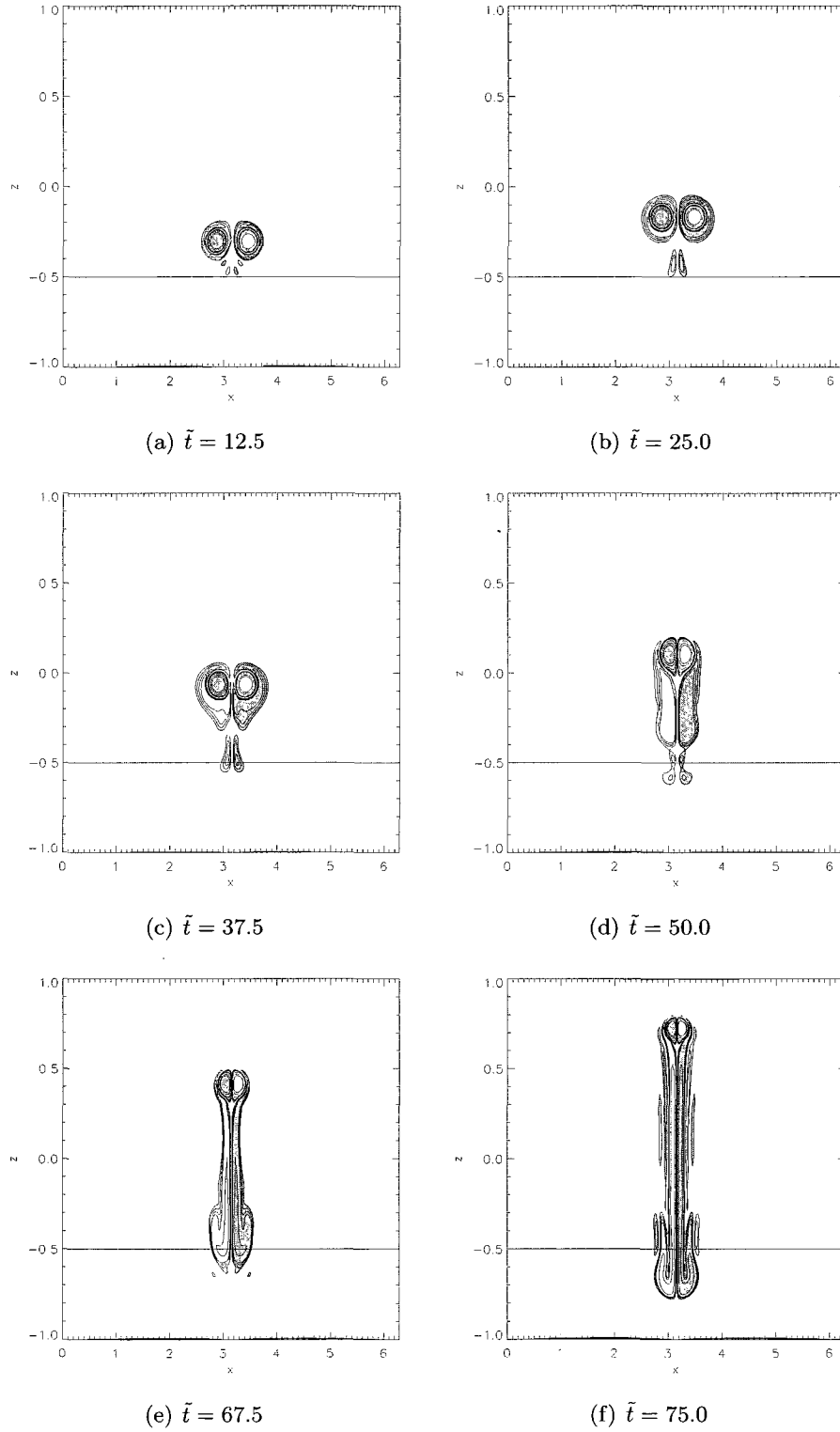


Figure V.3: Contours of vorticity for the single layer case with $\bar{F}_r = 4$ and a resolution of 256x256.

The vertical location of the vortex pair is determined by finding the location of the point of maximum vorticity. This method effectively tracks the vortex pair until the pair begins to disintegrate. As disintegration begins other points of high vorticity arise and the center can no longer be tracked easily. Time histories of the vertical position of the vortex pair are provided in figure V.4 for the same case of table V.2. Again the lower resolution case adequately predicts the correct behavior of the vortex pair, until the pair has reached the upper boundary.

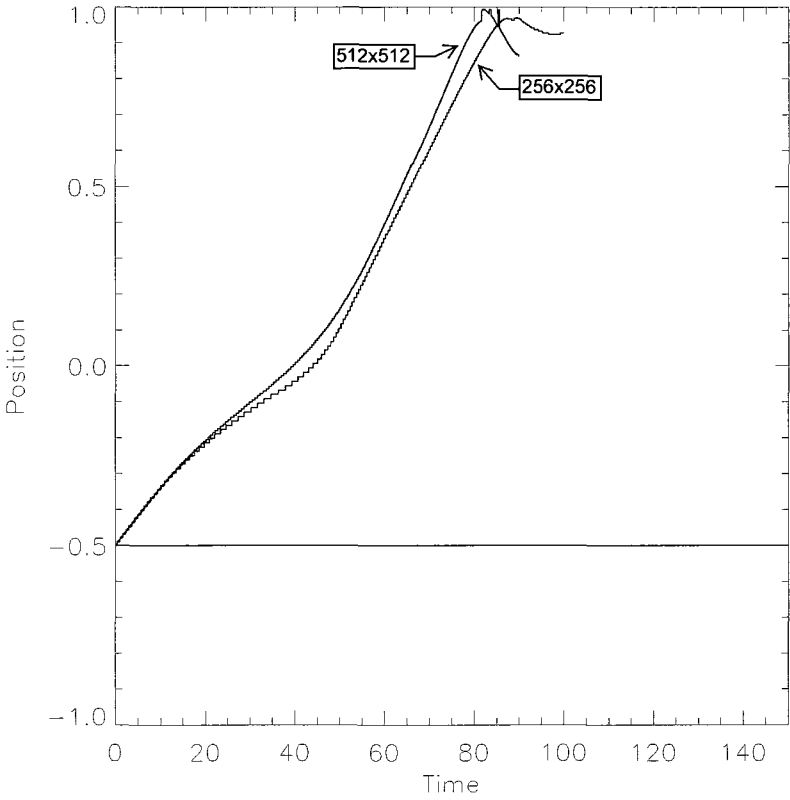


Figure V.4: Time history of vertical position of the vortex pair for two resolutions.

Mixing within a vortex

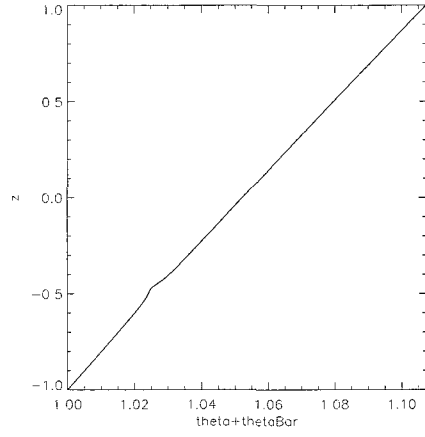
The velocity field of the initial vortex is an overturning flow, and the mean state is stably stratified. This means that the vortex flow acts to move heavier flow to the top and lighter fluid to the bottom, creating a statically unstable environment. If the vortex is relatively weak, then this static instability causes the vortex to disintegrate into internal waves. This is the mechanism that dominates the dynamics for $\overline{F}_r < 1$.

For large values of \overline{F}_r , the vortex is strong enough for centripetal acceleration to overcome the gravitational effect and stabilize the motion, allowing the vortices to remain coherent. However, even with coherent vortices, there is tremendous mixing within each vortex, very quickly resulting in a well-mixed vortex core. This can be seen in figure V.5, which shows a sequence of vertical profiles of total potential temperature at a horizontal position chosen to correspond to the initial position of the center of the left vortex. Note in figure V.5 that initially the potential temperature increases linearly, indicating static stability. As time progresses however, the region where the vortex resides (near $z = -0.5$) becomes complicated and finally reaches a state where the potential temperature inside the vortex is constant. This constant temperature state can be seen more clearly later in the vortex motion, shown in figure V.6. Note that a constant value of potential temperature is neutrally (statically) stable. Hence, before the vortex pair has moved significantly, it has become a fully mixed region of fluid. This fact was also indicated by Garten, et. al. [4].

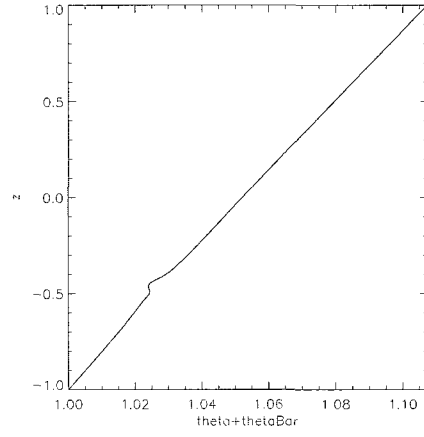
The mixing process can be seen more clearly in figures V.7 and V.8, which show contours of total potential temperature. These contours show that the vortex motion has caused streams of fluid of different temperature to be rolled up in a spiral pattern, allowing molecular dissipation to smooth out the difference very rapidly. However, the potential temperature never reaches a perfectly mixed state, evidenced by the continued presence of distinct contours throughout the life of the vortex.

After the initial mixing process, the vortex pair moves upward in a manner very similar to a vortex pair in constant density flow. The two vortices move closer together, as they do when ρ is constant. However one significant difference here is the temperature inside each vortex. The fluid that was entrained within each vortex in the early mixing stage remains

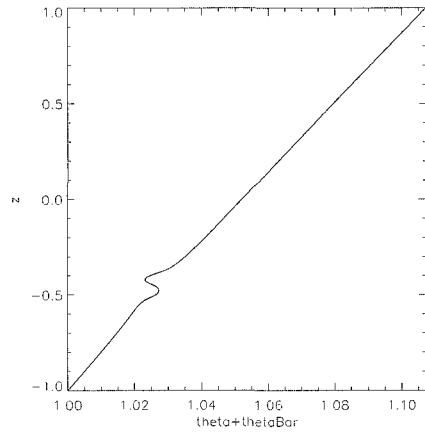
within the vortex and is forced to move upwards with the vortex. This can be best seen in the time sequence of vertical profiles of the total potential in figure V.6. The profiles show clearly that the well-mixed core of the vortex retains the potential temperature that it had when initiated, rising as a cold volume of fluid in increasingly warmer surroundings. This suggests that the motion of the vortex must overcome not only viscosity but also the negative buoyancy, as the entrained fluid is heavier than its surroundings. Later results will show indeed that in some cases the vortex pair ceases to ascend and begins to descend, apparently unable to resist the buoyant force.



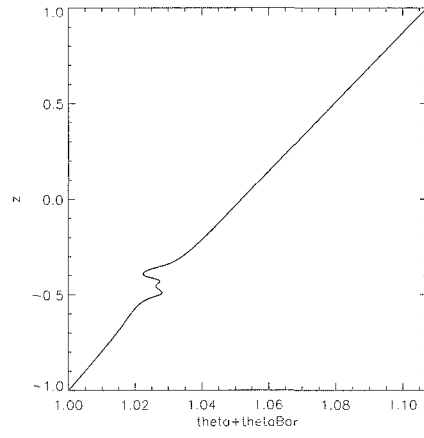
(a) $\tilde{t} = 0.5$



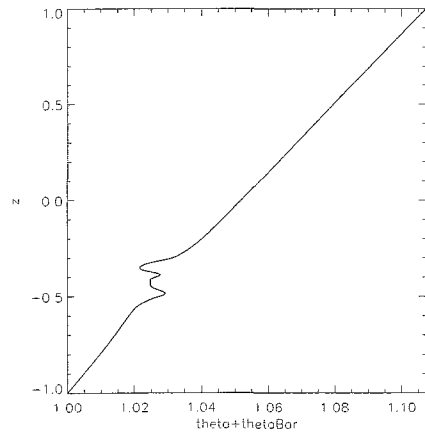
(b) $\tilde{t} = 1.0$



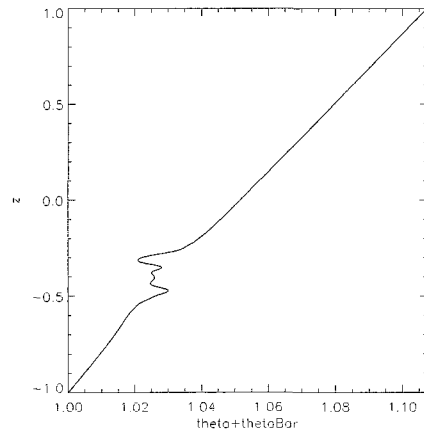
(c) $\tilde{t} = 2.0$



(d) $\tilde{t} = 3.0$

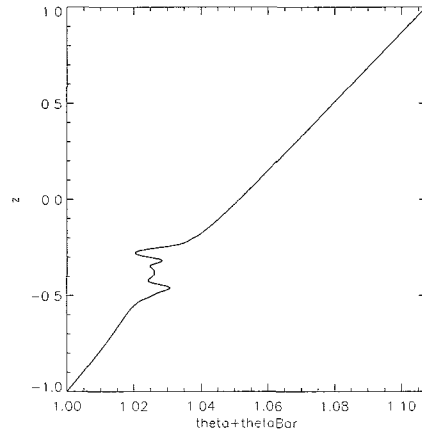


(e) $\tilde{t} = 4.5$

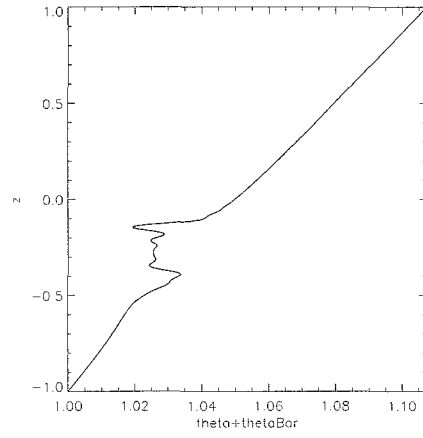


(f) $\tilde{t} = 6.0$

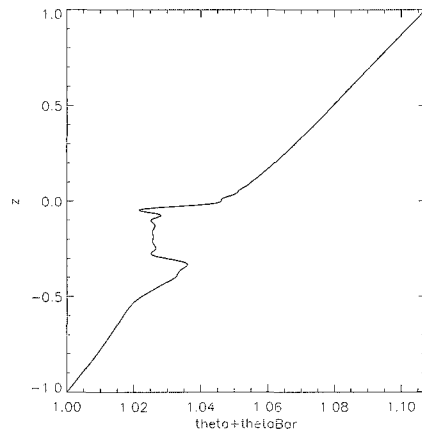
Figure V.5: Total potential temperature for the single layer case with $\overline{F}_r = 4$, a resolution of 512x512 and a vertical slice at $\tilde{x} = 2.9575$



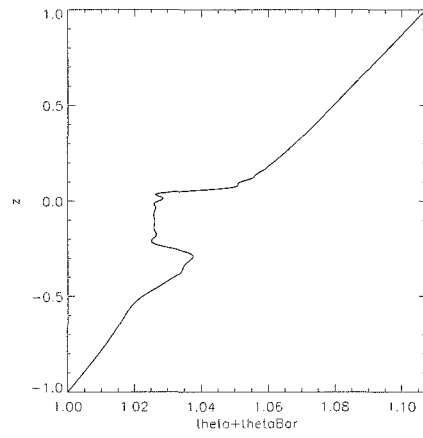
(a) $\tilde{t} = 7.5$



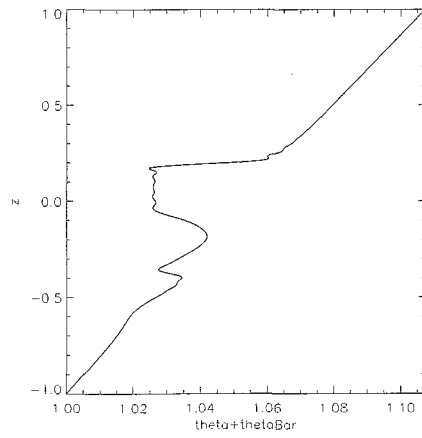
(b) $\tilde{t} = 15.0$



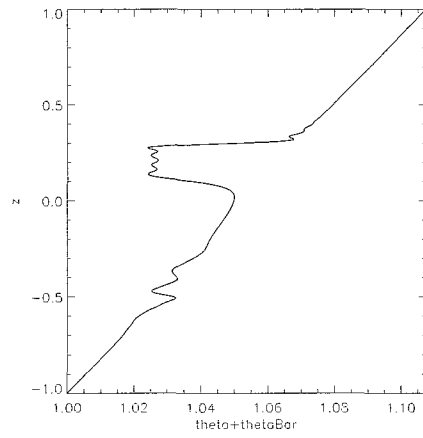
(c) $\tilde{t} = 22.5$



(d) $\tilde{t} = 30$



(e) $\tilde{t} = 45.0$



(f) $\tilde{t} = 52.5$

Figure V.6: Total potential temperature for the single layer case with $\overline{F}_r = 4$, a resolution of 512x512 and a vertical slice at $\tilde{x} = 2.9575$

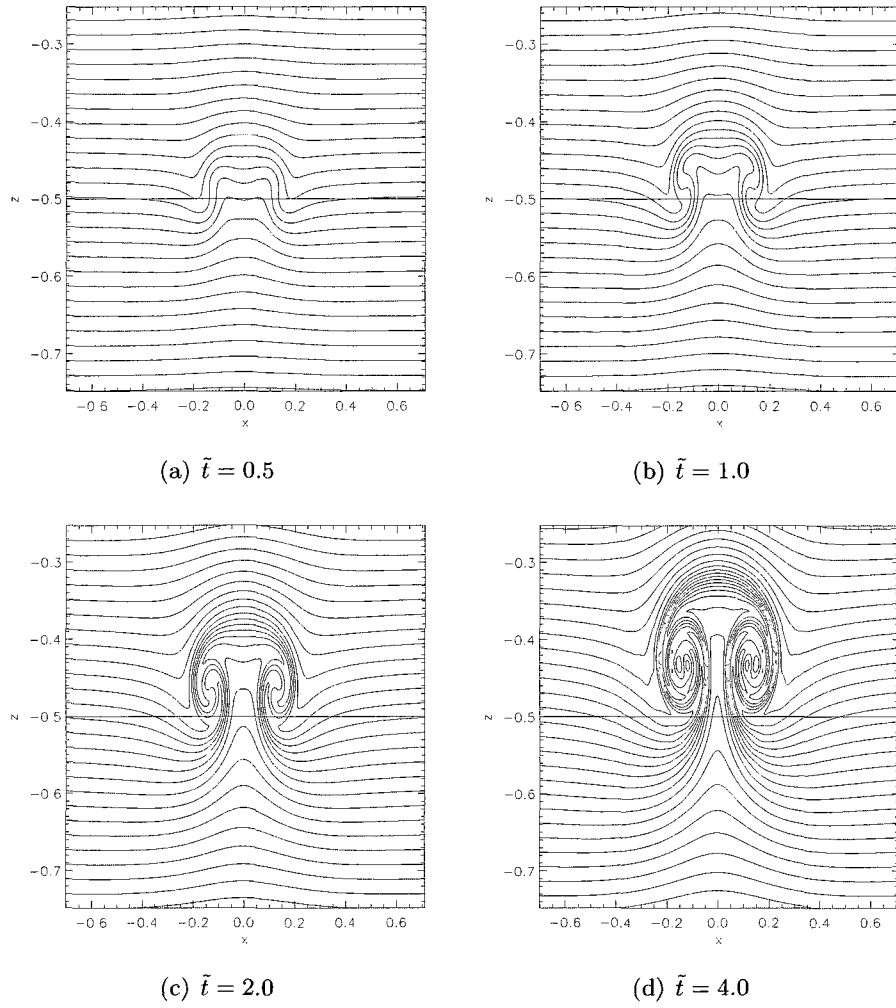
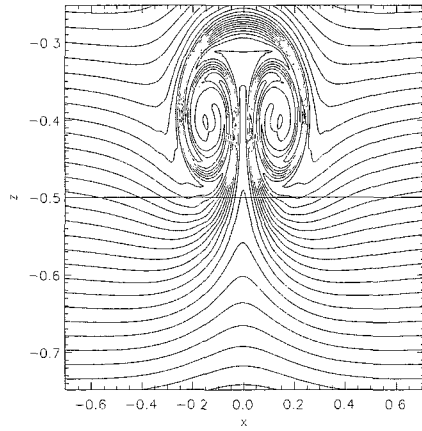
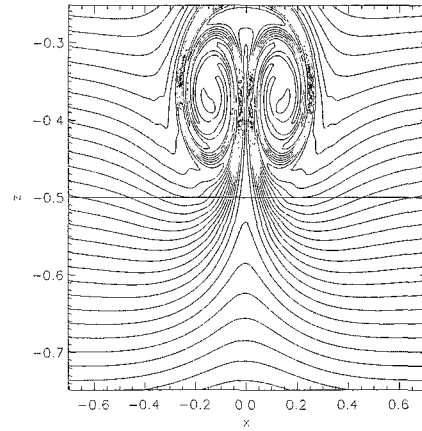


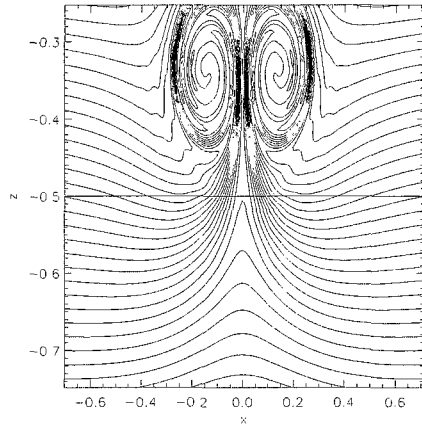
Figure V.7: Contours of total potential temperature for the single layer case with $\overline{F}_r = 4$ and a resolution of 512x512.



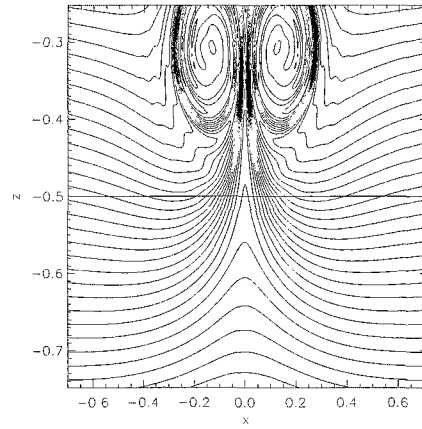
(a) $\tilde{t} = 6.0$



(b) $\tilde{t} = 8.0$



(c) $\tilde{t} = 12.0$



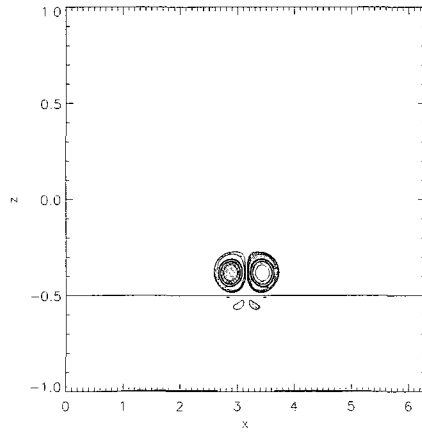
(d) $\tilde{t} = 16.0$

Figure V.8: Contours of total potential temperature for the single layer case with $\overline{F}_r = 4$ and a resolution of 512x512.

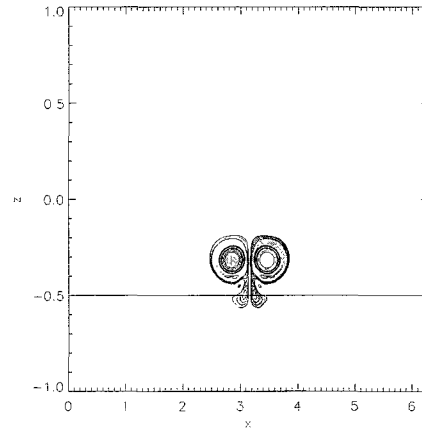
Results for two typical cases are shown in figures V.9 through V.12. The alternate Froude number is $\bar{F}_r = 2$ (figures V.9 and V.10) and $\bar{F}_r = 1.5$ (figures V.11 and V.12). Each frame in figures V.9- V.12 show contours of vorticity for one time value, and the solid line across each figure represents the vertical position of the initial vortices. The last frame in figures V.10 and V.12 show a time history of the vertical position of the vortex pair. This time history shows that the vortex pair for these parameters begins to ascend slowly, but then descends. For $\bar{F}_r = 2$, the strength of the vortex pair is still great enough to regain upward propagation. This is clearly seen in the final frame of figure V.10. However, with $\bar{F}_r = 1.5$ the strength of the vortex pair is not sufficient to overcome the buoyant forces on the vortex pair. In contrast to the case with $\bar{F}_r = 2$ this case shows that the vortex pair continues its descension past the initial release point. Interestingly, the vortex pair appears to be asymptotically approaching its original position for large times. This happens when the strength of the vortex pair has withered, and the remaining effect is buoyancy: merely cold patches of the entrained fluid oscillating about the original equilibrium position, slowly dissipating energy.

$\bar{F}_r = 2$ Low Resolution Parameters
$F_r = 1$
$Re = 1,000,000$
$G = 0.028$
$Res = 256 \times 256$

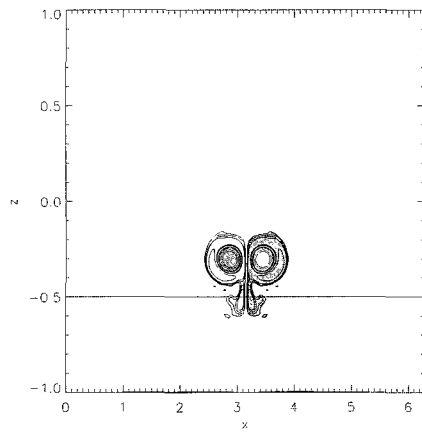
Table V.3: $\bar{F}_r = 2$ Low resolution parameter table



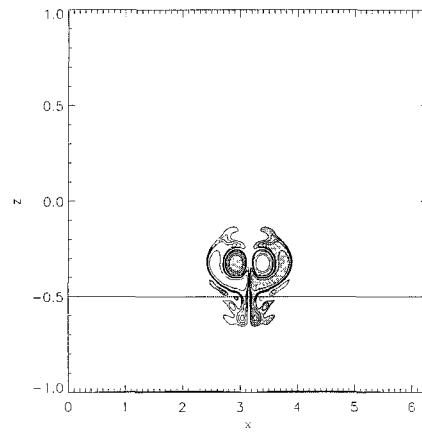
(a) $\tilde{t} = 15.0$



(b) $\tilde{t} = 30.0$



(c) $\tilde{t} = 45.0$



(d) $\tilde{t} = 60.0$

Figure V.9: Contours of vorticity for the single layer case with $\overline{F}_r = 2$ and a resolution of 256x256.

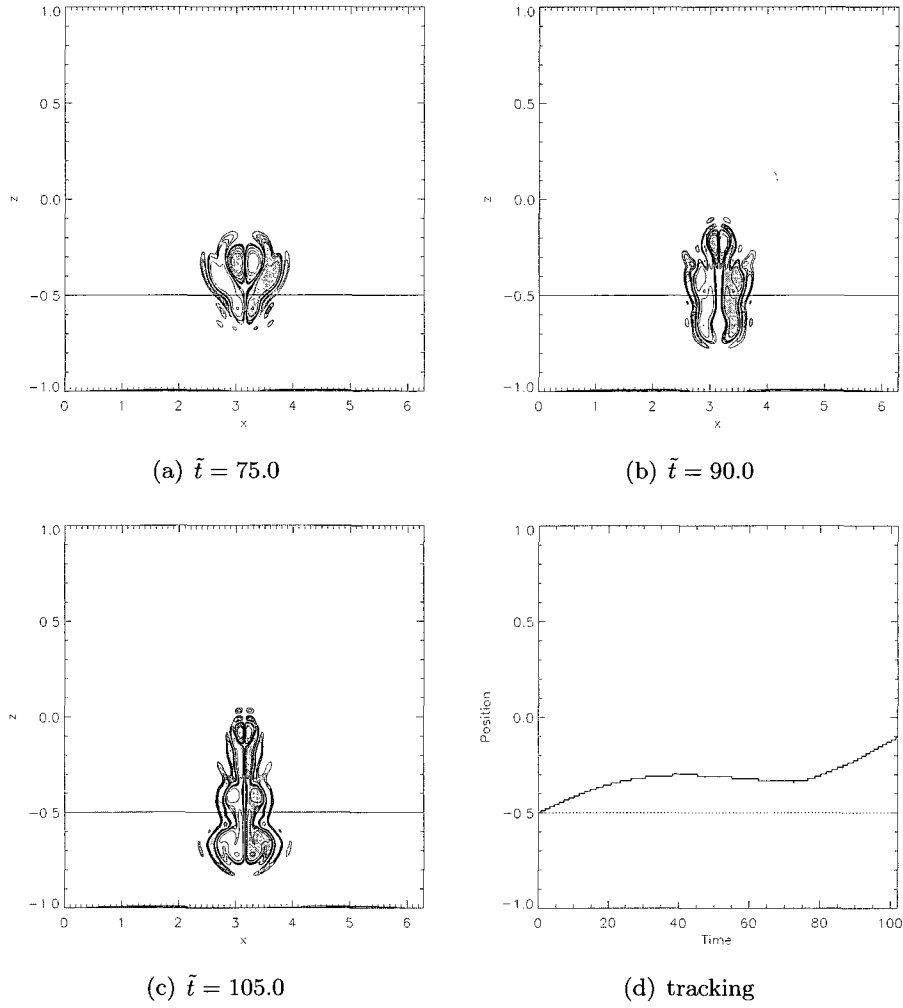
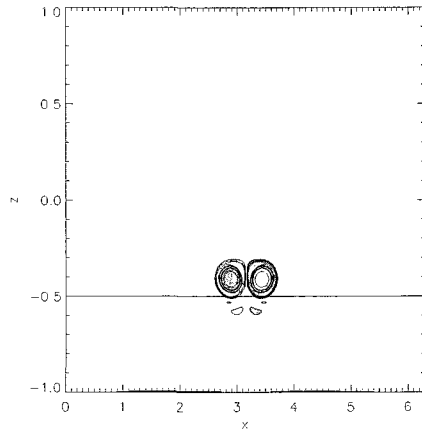


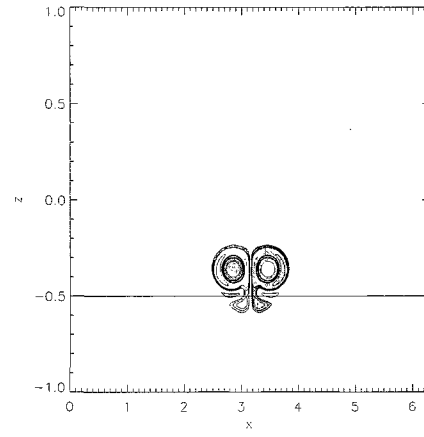
Figure V.10: Contours of vorticity for the single layer case with $\overline{F}_r = 2$ and a resolution of 256x256.

$\overline{F}_r = 1.5$ Low Resolution Parameters
$F_r = 1$
$Re = 1,000,000$
$G = 0.021$
$Res = 256 \times 256$

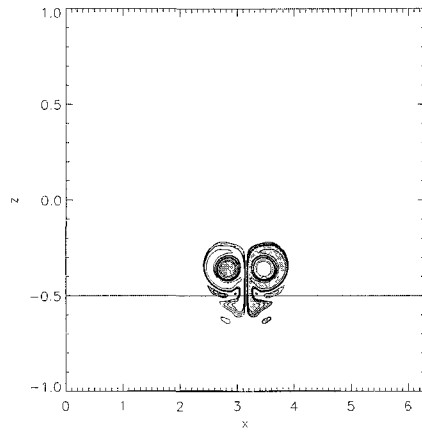
Table V.4: $\overline{F}_r = 1.5$ Low resolution parameter table



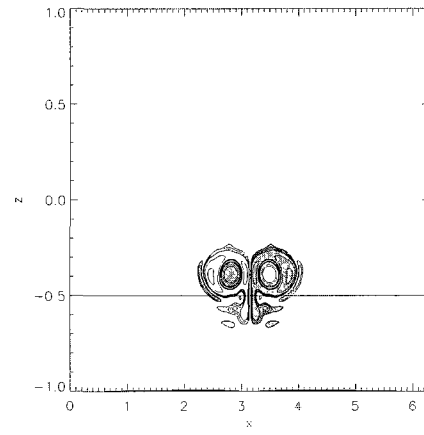
(a) $\tilde{t} = 15.0$



(b) $\tilde{t} = 30.0$



(c) $\tilde{t} = 45.0$



(d) $\tilde{t} = 60.0$

Figure V.11: Contours of vorticity for the single layer case with $\overline{F}_r = 1.5$ and a resolution of 256x256.

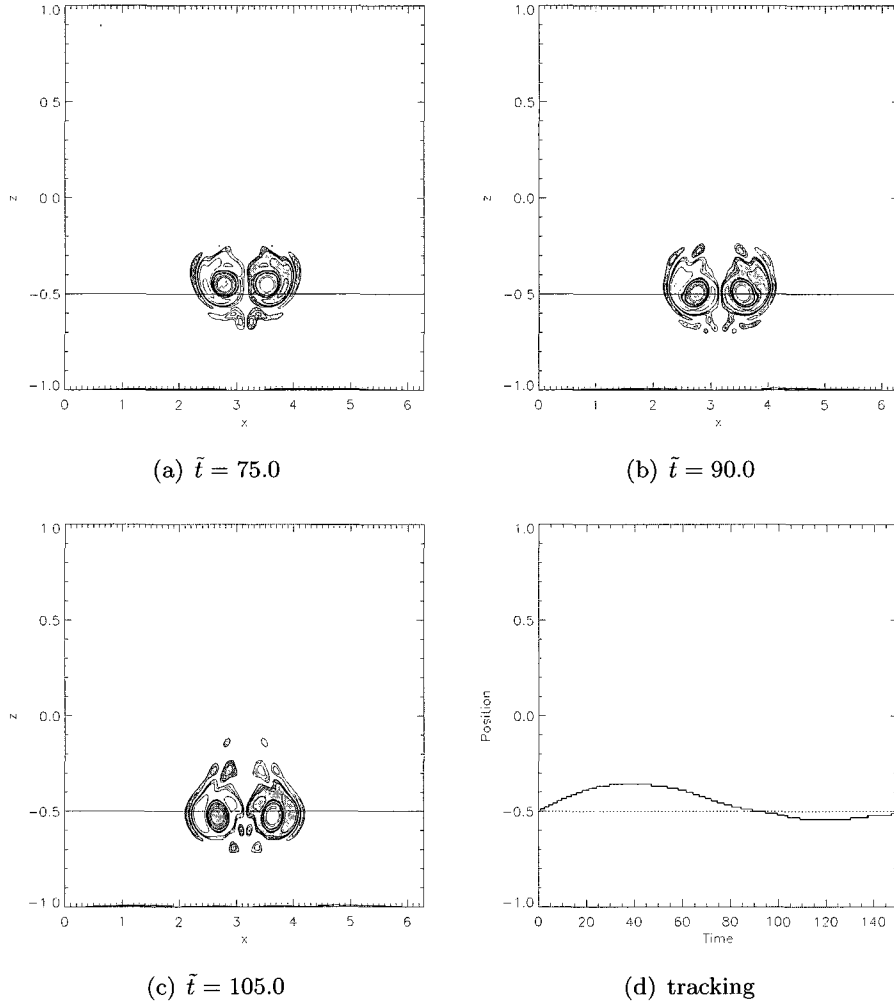


Figure V.12: Contours of vorticity for the single layer case with $\bar{F}_r = 1.5$ and a resolution of 256x256.

Figure V.13 shows the time histories of the vertical position of the vortex pair for several different values of \bar{F}_r . As the strength of the initial vortex is increased, the maximum height that the pair will achieve is increased. Finally, for $\bar{F}_r = 4$ the strength is great enough that the vortex pair achieves a constant vertical speed, maintaining this vertical motion until the top of the computational domain is reached.

A final single-layer case is shown in figure V.14. The initial strength for the vortex pair is weak, chosen such that $\bar{F}_r = 0.5$. Although \bar{F}_r is below the critical value of unity, the vortex pair still has minimal vertical propagation before dissipating into internal waves. Hence, \bar{F}_r is not quite the steep transition reported by Garten, et. al.

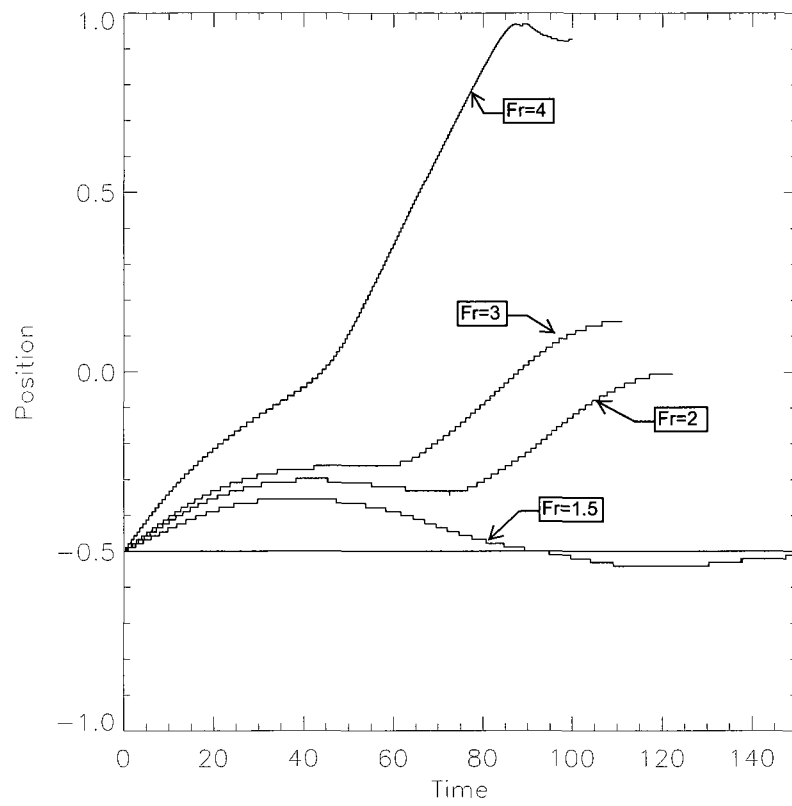


Figure V.13: Max vorticity location for single layer cases.

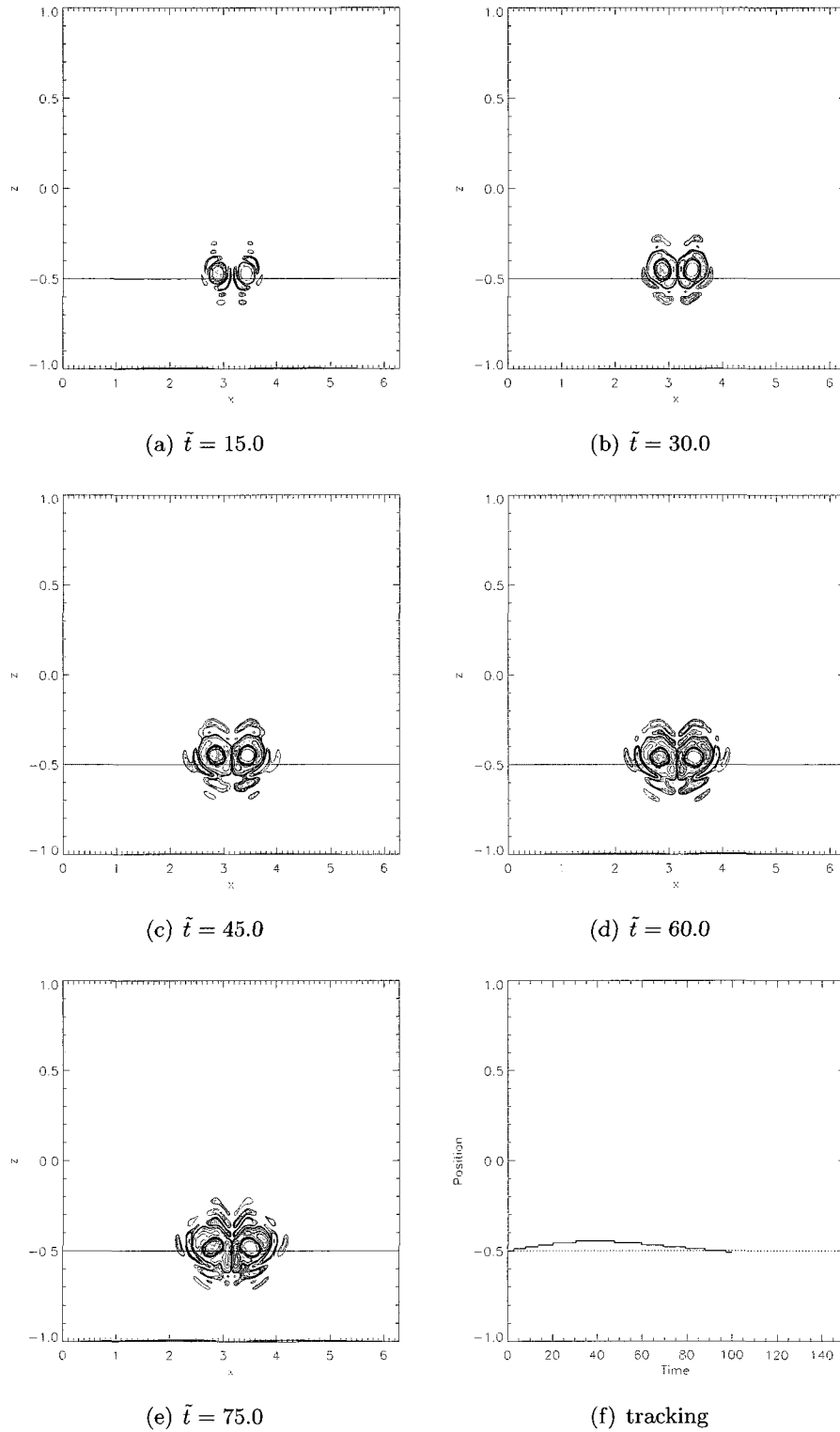


Figure V.14: Contours of vorticity of single layer with $\overline{F}_\tau = 0.5$ and a resolution of 256x256.

Two Layers

Now consider two-layer flow, as described in the introduction. Each layer has a constant value of N , and the horizontal interface between the layers is a density gradient interface, where the density is continuous, but the density gradient is discontinuous. For all cases considered here, the vortex pair is released in the lower layer and allowed to propagate vertically toward the interface.

The results may be categorized again by the value of the alternate Froude number in each layer. If \overline{F}_r in the lower layer is less than unity, then the vortex pair will not propagate very far, and never reaches the interface. The results show that the vortex disintegrates into internal waves, as with the single layer. This case will not be considered further.

If \overline{F}_r in the lower is greater than unity, but only slightly greater, then the vortex pair still will not ascend far enough to reach the interface. Hence, only strong vortices (larger values of \overline{F}_r) are considered here, which do reach the interface.

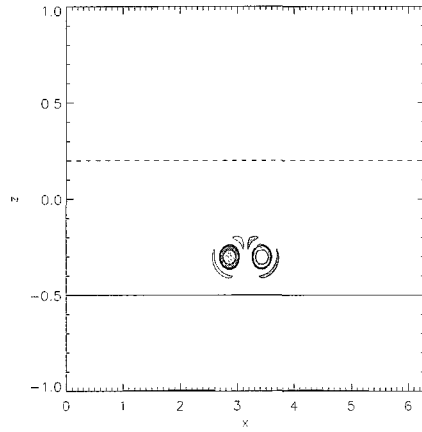
The value of N in Earth's atmosphere increases at the tropopause by a factor of two. This means that the alternate Froude number *decreases* in value by the same factor. Hence a vortex pair in the lower layer with $\overline{F}_r = \frac{W_0}{N_1 b_0}$ greater than unity may reach the upper layer where $\overline{F}_r = \frac{W_0}{N_2 b_0}$ is less than unity. Hence it would appear that there are two distinct cases depending on the value of \overline{F}_r in the upper layer.

However, the critical Froude number of unity only applies to an impulsively started vortex in a stratified flow, before any mixing has occurred. Once the vortex flow becomes fully mixed, the value of \overline{F}_r may be less than unity and the vortex does not immediately dissipate into waves.

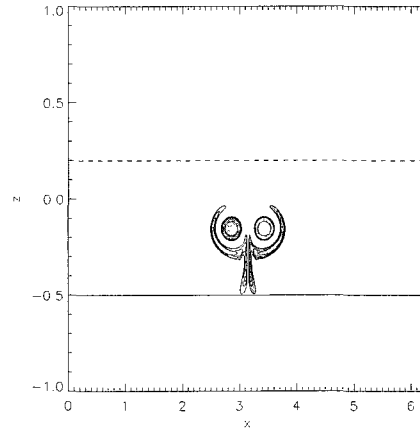
Results for a relatively strong vortex (\overline{F}_r of 4) are shown in figure V.15, again using contours of vorticity for a sequence of times. The position of the interface is indicated with a horizontal dashed line, and again the initial position of the vortex pair is indicated with a horizontal solid line. The results in figure V.15 use the higher resolution (512x512). These results correspond to figure V.2 for the single layer case. Figure V.17 shows a time history of the vertical position of the vortex pair for both the two layer and single layer case. Figure V.15 shows that this strong vortex pair moves through the interface with only

minor changes in the behavior of the flow. There are almost no differences between the two layer images in figure V.15 and the single layer images in figure V.2. This is because the vortex is already fully mixed when it reaches the interface, and therefore mostly isolated from the surrounding fluid. The fluid in the upper layer does not get entrained significantly into the vortex, hence the only effect on the vortex pair is the increased buoyant force due to the lower density fluid in the upper layer. The effect of this buoyant force can be seen in the time history of vertical position in figure V.17. The vertical position for the two cases is nearly identical until the interface is reached. Then the vortex pair in the two layer case cannot keep up with the single layer case, and does not reach the same final height. This difference is due mostly to the increased buoyant force slowing down the vortex pair in the two layer case.

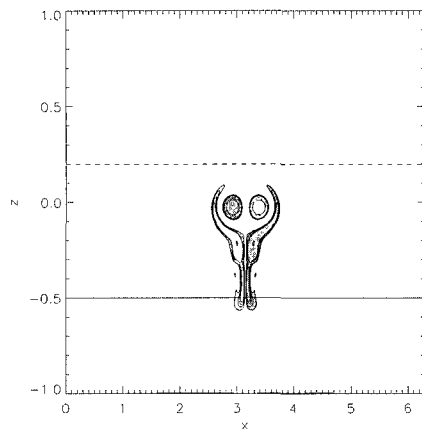
Figure V.16 shows the same case as figure V.15 except now with the lower resolution (256x256). Once again, the lower resolution case shows the same basic dynamics, with some differences mostly in the wake region behind the vortex pair.



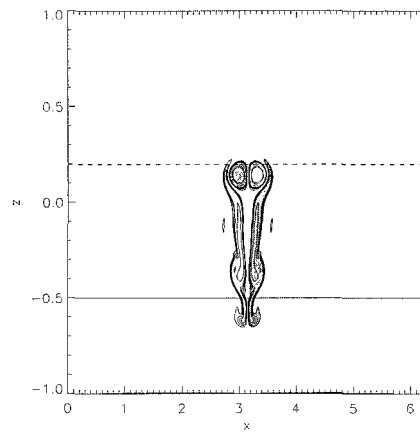
(a) $\tilde{t} = 12.5$



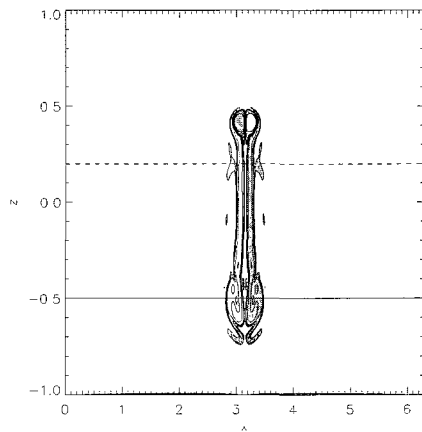
(b) $\tilde{t} = 25.0$



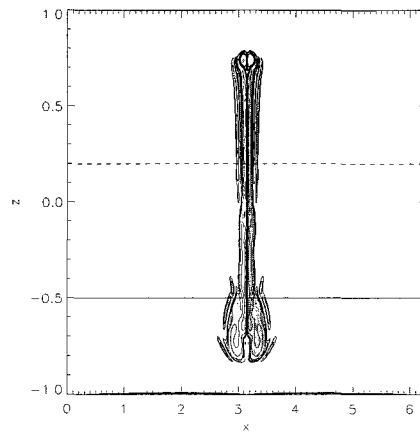
(c) $\tilde{t} = 37.5$



(d) $\tilde{t} = 50.0$

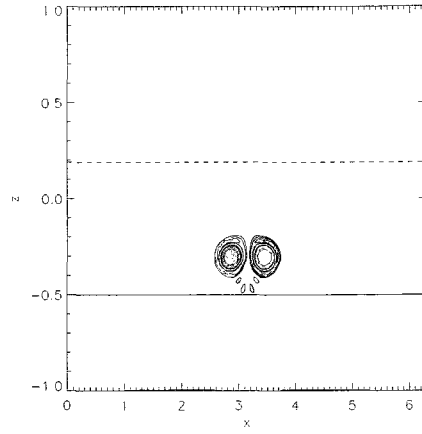


(e) $\tilde{t} = 62.5$

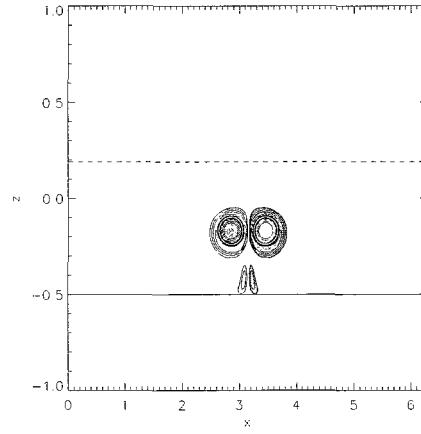


(f) $\tilde{t} = 75.0$

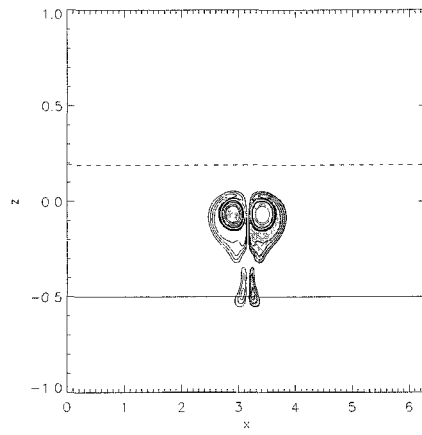
Figure V.15: Contours of vorticity for the two layer case with $\overline{F}_r = 4$ and a resolution of 512x512.



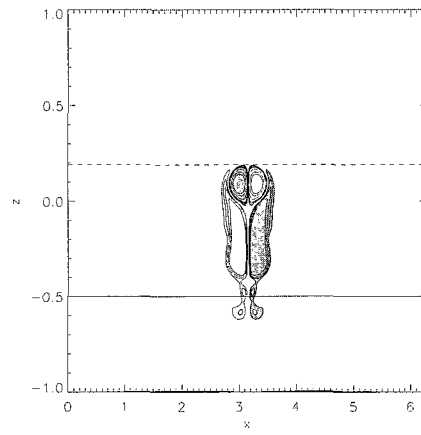
(a) $\tilde{t} = 12.5$



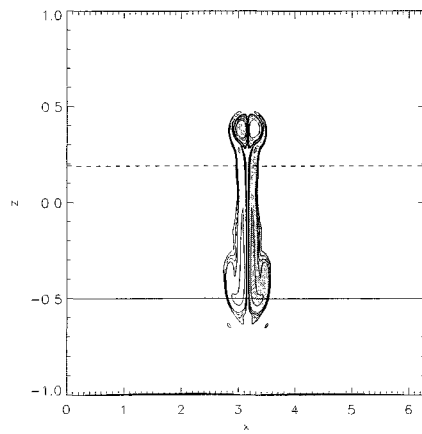
(b) $\tilde{t} = 25.0$



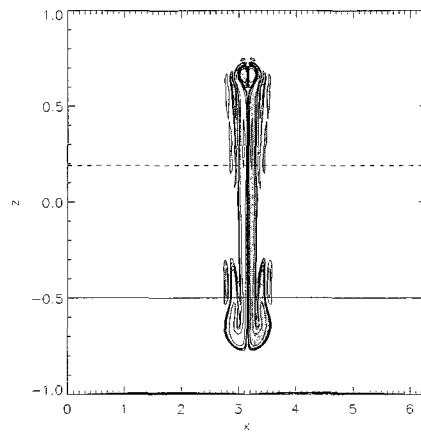
(c) $\tilde{t} = 37.5$



(d) $\tilde{t} = 50.0$



(e) $\tilde{t} = 67.5$



(f) $\tilde{t} = 75.0$

Figure V.16: Contours of vorticity for the two layer with $\overline{F}_r = 4$ and a resolution of 256x256.

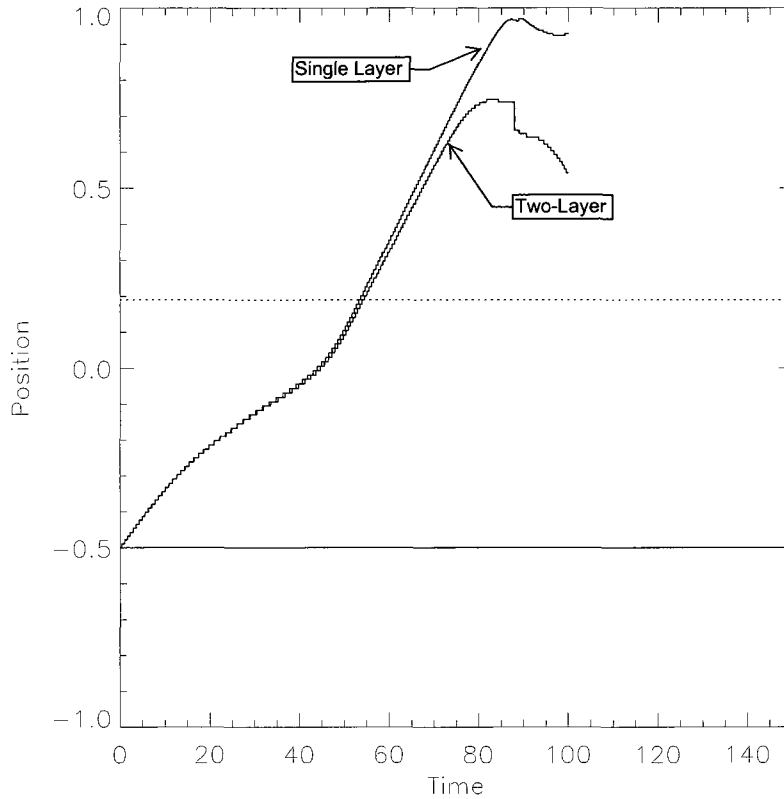
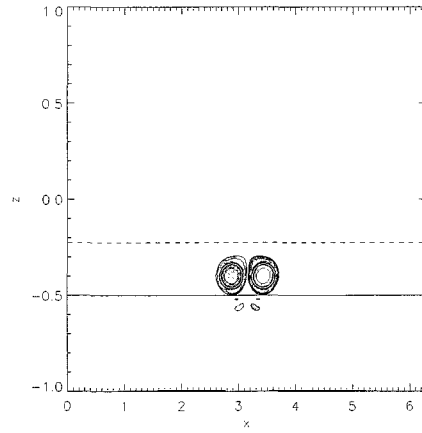


Figure V.17: $\bar{F}_r = 4$ single layer and $\bar{F}_r = 4$ two-layer. The single layer case clearly has a higher vertical displacement as it collides with the top boundary, where the two-layer case only reaches $\hat{z} = 0.75$.

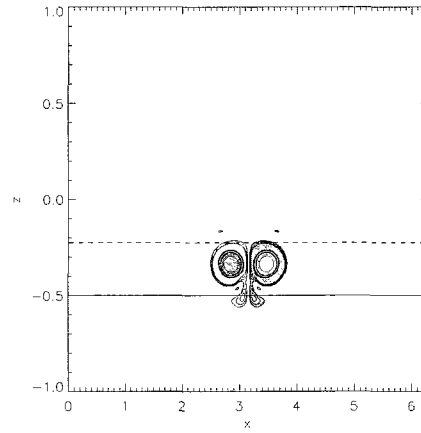
A second two-layer case is shown in figures V.18 and V.19 for a weaker vortex pair, now with $\bar{F}_r = 2$. This weak vortex does not reach the interface if the interface is maintained at the same position as figure V.15 and V.16 ($z \approx 0.2$), so the interface for this second case has been moved down to $z = -0.225$. For this lower Froude number, even in a single layer, the vortex begins to ascend, but then descends as the vortex pair evolves. The vortices then move closer together, increasing the dynamic effect that causes the upward motion, and the vortices then ascend again. When the interface is located nearby, this process evolves near the interface, resulting in an interaction with the interface. The vorticity patterns in figures V.18 and V.19 shows this interaction first at the top of the vortices. This pattern indicates that the vortices are creating waves in the upper layer, which doesn't happen without the interface. This behavior drains energy away from the vortex pair, and causes the

vortex pair to descend further. Figure V.20 shows the time history of the vertical position of the vortex pair for this case, along then the analogous single-layer case. Figure V.20 shows that the vortex pair with two layers descends further, but does recover and ascend once more, finally penetrating the interface. However, figure V.19 shows that the vortex pair that actually penetrates the interface is much reduced in size and strength than the analogous single-layer case. Furthermore, the flow is much different, being mostly composed of an internal wave pattern that was created before penetration.

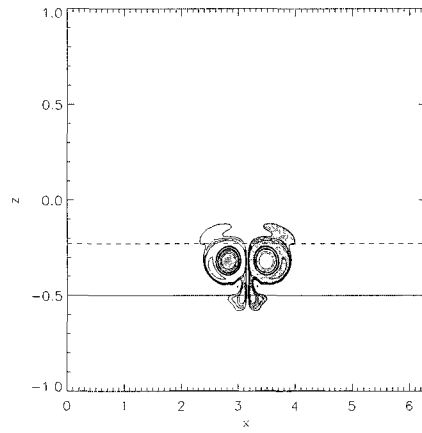
This case with lower \overline{F}_r is different than the high \overline{F}_r case because the adjustment period where the vortices move closer together happened in the vicinity of the interface. This appears to be the primary manner in which these results can be categorized. If the vortex pair can become fully mixed and then the vortices reach this equilibrium where they are close together, then the dynamics proceeds as with a single layer, only different as a result of the somewhat different buoyant force. However, if the vortex pair is created near the interface, the vortices adjust differently, release most of their energy as internal waves, and finally result in a much different overall flow. Hence on average the interface does act as a barrier to this form of kinetic energy, but only if the flow is not fully mixed. The interface will therefore treat vortices created nearby differently than vortices created far from the interface.



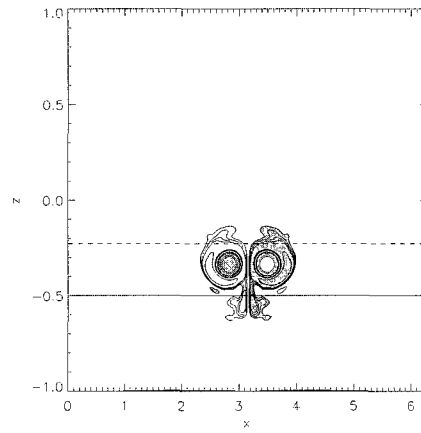
(a) $\tilde{t} = 12.5$



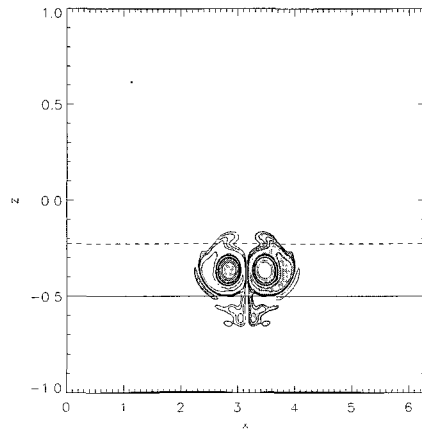
(b) $\tilde{t} = 25.0$



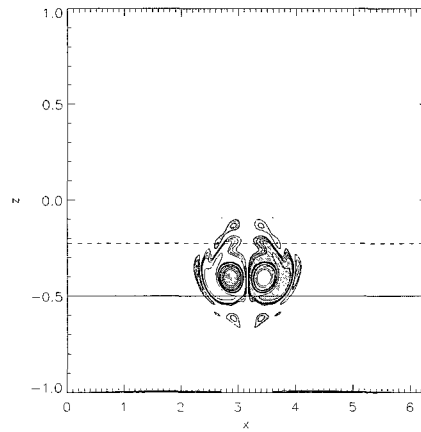
(c) $\tilde{t} = 37.5$



(d) $\tilde{t} = 50.0$

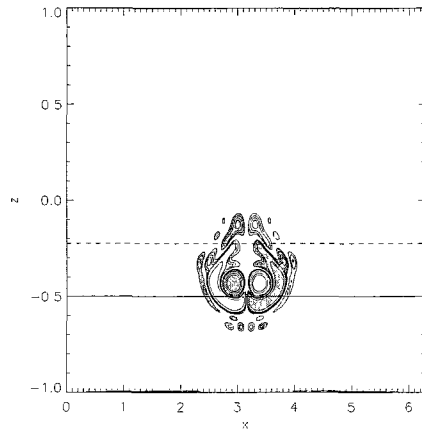


(e) $\tilde{t} = 67.5$

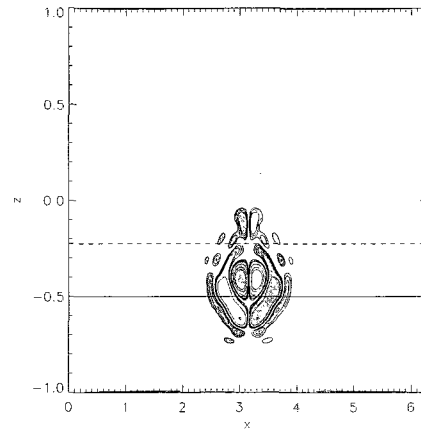


(f) $\tilde{t} = 75.0$

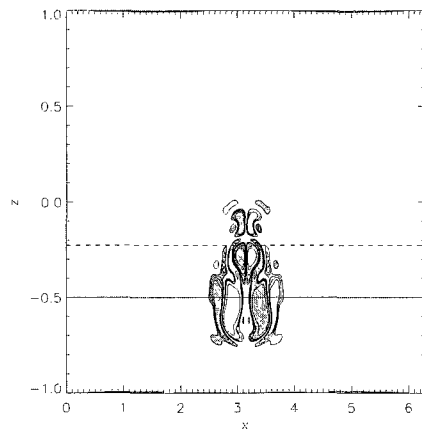
Figure V.18: Contours of vorticity for the two layer case with $\overline{F_r} = 2$ and a resolution of 256x256.



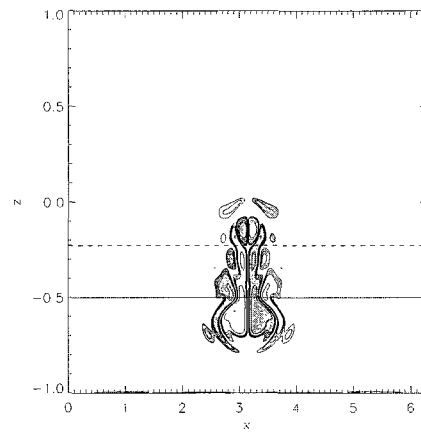
(a) $\bar{t} = 87.5$



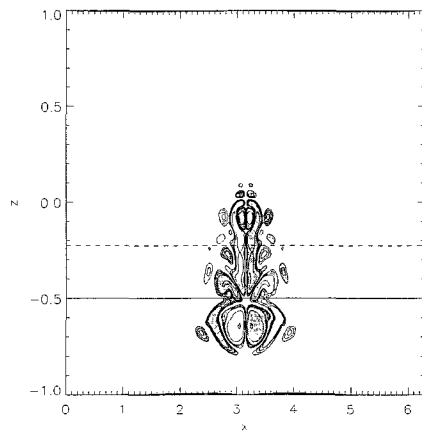
(b) $\bar{t} = 100.0$



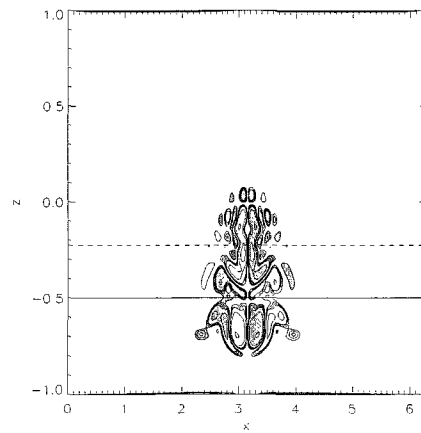
(c) $\bar{t} = 112.5$



(d) $\bar{t} = 120.0$



(e) $\bar{t} = 137.5$



(f) $\bar{t} = 150.0$

Figure V.19: Contours of vorticity for the two layer case with $\overline{F}_r = 2$ and a resolution of 256x256.

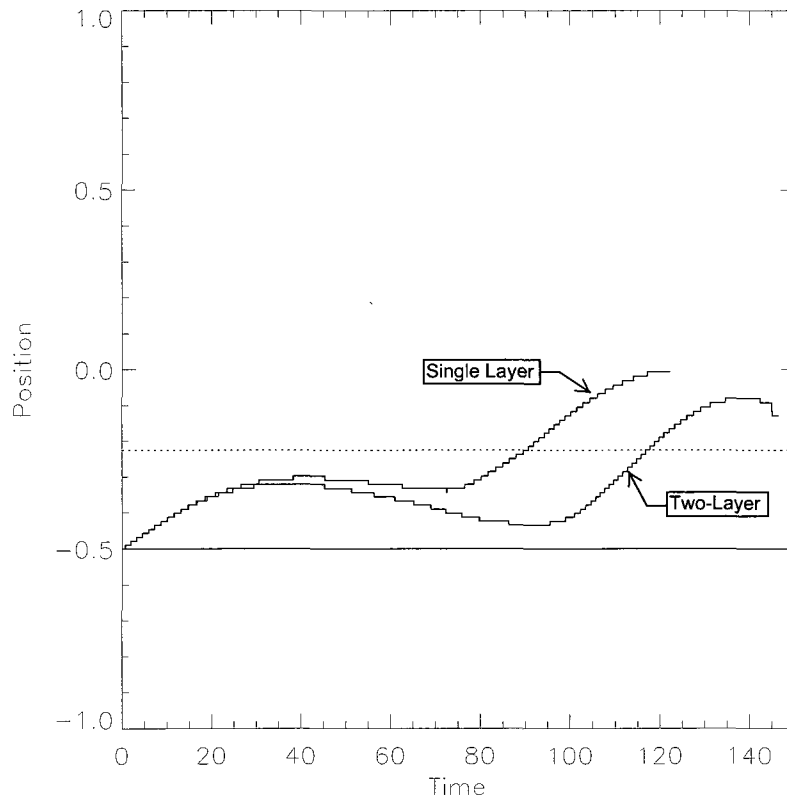


Figure V.20: $\overline{F}_r = 2$ single layer and $\overline{F}_r = 2$ two-layer. The single layer case clearly has a higher vertical displacement as it collides with the top boundary, where the two-layer case only reaches $\hat{z} = 0.75$.

Conclusions

The dynamics of a vortex pair in a stratified atmosphere near a density gradient interface is considered here using direct numerical simulations. The vortex pair was released below the interface and allowed to propagate vertically toward the interface. The results show that strong vortices propagate through the interface without much change in their dynamics. Weaker vortices will dissipate energy when they reach the interface and although a remnant of the vortex pair transits the interface, it does not achieve the same altitude that it would have without the interface. Overall, the interface is not a barrier to vortex pairs with fully developed cores. However, if the interface between the layers is sufficiently close so that interaction occurs before the core becomes well mixed, the vortex is dramatically affected. This interaction with the interface causes the vortex pair to radiate energy as internal waves above the interface. Hence, the interface is a barrier to vortex pairs created nearby.

Bibliography

- [1] Claudio Canuto, M. Yousuff Hussaini, Alfio Quarteroni and Thomas A. Zang 1988 *Spectral Methods in Fluid Dynamics*. Dover Publications, Inc, New York.
- [2] DONALD N. SLINN AND J. J. RILEY 1998 A model for the Simulation of Turbulent Boundary Layers in an Incompressible Stratified Flow. *Journal of Computational Physics*. 550–602.
- [3] FREDERICK S. SHERMAN 1990 *Viscous Flow*. McGraw-Hill, Inc, New York.
- [4] J. F. GARTEN, S. ARENDT, D.C. FRITTS AND J. WERNE 1984 Dynamics of Counter-rotating vortex pairs in stratified and sheared environments. *J. Fluid Mech.* 189-236.
- [5] J. K. WOLFF AND R. D. SHARMAN 2008 Climatology of upper-level turbulence over the continuous United States. *J. Appl. Meteor. Climatol.* **47**, 2198–2214.
- [6] JOHN P. BOYD 2001 *Chebyshev and Fourier Spectral Methods*. Dover Publications, Inc, Mineola, NY, 2nd Edition.
- [7] JOHN P. MCHUGH 2008 Mean Flow generated by an internal wave packet impinging on the interface between two layers of fluid with continuous density. *Theoretical and Computational Fluid Dynamics*. **22** 107–123.
- [8] JOHN P. MCHUGH 2009 Internal waves at an interface between two layers of differing stability. *J. Atmos. Sci.* **66**, 1845–1855.
- [9] J. P. MCHUGH, G. Y. JUMPER, M. CHUN 2008 Balloon thermosonde measurements over Mauna Kea, and comparison with seeing measurements. *Pub. Astro. Soc. Pac.* **120**, 1318–1324.

- [10] J. P. MCHUGH, I. DORS, G. Y. JUMPER, J. ROADCAP, E. MURPHY, AND D. HAHN
2008 Large variations in balloon ascent rate over Hawaii. *J. Geo. Res.* **113**.
- [11] GEORGE EM KARNIADAKIS, MOSHE ISRAELI, AND STEVEN A. ORSZAG 1991 High-
Order Splitting Methods for the Incompressible Navier-Stokes Equations. *Journal of
Computational Physics* **97**, 414–443.
- [12] P. G. SAFFMAN 1972 The motion of a vortex pair in a stratified atmosphere. *Studies
in Applied Math* **51**, 107–119.
- [13] R. M. WORTHINGTON 1998 Tropopausal turbulence caused by the breaking of moun-
tain waves. *J. Atmos. Sol.-Terr. Phy.* **60**, 1543–1547.
- [14] R. S. SCORER 1949 Theory of waves in the lee of mountains. *Q. J. Roy. Met. Soc.* **75**,
41–56.
- [15] ROBERT G. VOIGT, DAVID GOTTLIEB AND M. YOUSUFF HUSSAINI 1984 Spectral
Methods for Partial Differential Equations. *Society for Industrial and Applied Mathe-
matics, Philadelphia*.
- [16] W. PARTL 1962 Clear air turbulene at the tropopause levels. *Navigation* **9**, 288–295.